The solar UV–x-ray spectrum from 1.5 to 2000 Å

2010 J. Phys. B: At. Mol. Opt. Phys. 43 232001

(http://iopscience.iop.org/0953-4075/43/23/232001)

Report Documentation Page

Form Approved
OMB No. 0704-0188

1. REPORT DATE **JUL 2010**	2. REPORT TYPE	3. DATES COVERED **00-00-2010 to 00-00-2010**

4. TITLE AND SUBTITLE **The solar UV-x-ray spectrum from 1.5 to 2000 A**	5a. CONTRACT NUMBER 5b. GRANT NUMBER 5c. PROGRAM ELEMENT NUMBER
6. AUTHOR(S)	5d. PROJECT NUMBER 5e. TASK NUMBER 5f. WORK UNIT NUMBER
7. PERFORMING ORGANIZATION NAME(S) AND ADDRESS(ES) **Naval Research Laboratory,Space Science Division,Washington,DC,20375**	8. PERFORMING ORGANIZATION REPORT NUMBER
9. SPONSORING/MONITORING AGENCY NAME(S) AND ADDRESS(ES)	10. SPONSOR/MONITOR'S ACRONYM(S) 11. SPONSOR/MONITOR'S REPORT NUMBER(S)

12. DISTRIBUTION/AVAILABILITY STATEMENT
Approved for public release; distribution unlimited

13. SUPPLEMENTARY NOTES

14. ABSTRACT
This review illustrates the potential of UV?x-ray spectroscopy for determining the physical conditions in the solar chromosphere, transition region and corona, and how spectroscopy can be used as a tool to understand the physical mechanisms governing the atmosphere. It also illustrates the potential for understanding transient events such as solar flares. This is a vast topic, and therefore the review is necessarily not complete, but we have tried to be as general as possible in showing in particular how solar spectra are currently being used to understand the solar upper atmosphere. The review is intended for non-solar physicists with an interest in spectroscopy as well as for solar physicists who are not specialists in spectroscopy.

15. SUBJECT TERMS

16. SECURITY CLASSIFICATION OF:			17. LIMITATION OF ABSTRACT	18. NUMBER OF PAGES	19a. NAME OF RESPONSIBLE PERSON
a. REPORT **unclassified**	b. ABSTRACT **unclassified**	c. THIS PAGE **unclassified**	**Same as Report (SAR)**	**24**	

Standard Form 298 (Rev. 8-98)
Prescribed by ANSI Std Z39-18

J. Phys. B: At. Mol. Opt. Phys. **43** (2010) 232001 (23pp) doi:10.1088/0953-4075/43/23/232001

TOPICAL REVIEW

The solar UV–x-ray spectrum from 1.5 to 2000 Å

G A Doschek[1] and U Feldman[2]

[1] Space Science Division, Naval Research Laboratory, Washington, DC 20375, USA
[2] Artep, Inc., 2922 Excelsior Spring Ct, Ellicott City, MD 21042, USA

E-mail: ufeldman@ssd5.nrl.navy.mil

Received 5 May 2010, in final form 28 July 2010
Published 12 November 2010
Online at stacks.iop.org/JPhysB/43/232001

Abstract
This review illustrates the potential of UV–x-ray spectroscopy for determining the physical conditions in the solar chromosphere, transition region and corona, and how spectroscopy can be used as a tool to understand the physical mechanisms governing the atmosphere. It also illustrates the potential for understanding transient events such as solar flares. This is a vast topic, and therefore the review is necessarily not complete, but we have tried to be as general as possible in showing in particular how solar spectra are currently being used to understand the solar upper atmosphere. The review is intended for non-solar physicists with an interest in spectroscopy as well as for solar physicists who are not specialists in spectroscopy.

(Some figures in this article are in colour only in the electronic version)

1. Overview: the solar UV–x-ray spectrum from 1.5 to 2000 Å

The solar atmosphere contains plasma at all temperatures ranging from its visible light surface (the photosphere, about 5500 K) up to coronal temperatures of about 1–3 $\times$ 10^6 K when the Sun is not producing flares. In a flare, temperatures as high as 20–40 $\times$ 10^6 K can be produced. The spectrum produced by the hot atmosphere extends from the UV into the x-ray region and is an emission line spectrum with free–free and free–bound continua. The emission lines produced are a reflection of the elements present in the atmosphere and their ionization stages. At temperatures above about 2 $\times$ 10^4 K the ion abundance (X^{+z}) of a particular element is determined by electron impact ionization of the ion competing with radiative and dielectronic recombination. Ionization equilibrium is often assumed in which case these competing processes balance, i.e.

$$N(X^{+z})Q^z = N(X^{+(z+1)})\left(\alpha_r^{(z+1)} + \alpha_d^{(z+1)}\right), \qquad (1)$$

where N is the number density of the X^{+z} ion, Q is the ionization rate coefficient (cm^3 s^{-1}) and α are the radiative and dielectronic recombination rate coefficients. These processes depend primarily on the electron temperature, although there is also some electron density dependence. Three-body recombination is negligible at the electron densities of the solar atmosphere, and above about 5 $\times$ 10^4 K radiative transfer effects on line profiles of resonance lines are small except for very abundant elements such as hydrogen. The emission lines produced above 5 $\times$ 10^4 K can for the most part be considered to be optically thin. The emission lines are produced mostly by electron impact excitation, although dielectronic recombination produces strong lines in the x-ray region below 10 Å and proton impact excitation and radiative recombination must also be considered.

The solar atmosphere element abundances are cosmic, i.e. they reflect the average element abundances in the Universe. About 92% of the atmosphere is hydrogen, about 8% is helium and about 0.2% is composed of mostly elements with atomic number $Z \leqslant 28$ (Ni). Because of the processes governing element formation in stars, it turns out that the most abundant light elements have even atomic numbers, i.e. carbon, oxygen, neon, magnesium, silicon, sulfur, argon, calcium, iron and nickel are significantly more abundant than elements such as boron, fluorine and phosphorus. Table 1 shows examples of photospheric (Asplund *et al* 2009) and coronal (Laming and Feldman 2000) abundances frequently adopted in analyses of solar spectra. Iron produces the

Table 1. Solar abundances.

Element	Photospheric abundance	Coronal abundance
H	12.00	12.00
He	10.93	10.93
C	8.43	8.52
N	7.83	7.92
O	8.69	8.83
Ne	7.93	8.11
Na	6.24	6.92–7.22
Mg	7.60	8.18
Al	6.45	7.09–7.39
Si	7.51	8.16
S	7.12	7.33
Ar	6.40	6.59
Ca	6.34	6.95–7.25
Fe	7.50	8.10
Ni	6.22	6.85

strongest high-temperature lines in the solar spectrum because it is the heaviest abundant element and the highest degrees of iron ionization stages are produced at the highest temperatures relative to the temperature sensitivities of the other elements. Above the atomic number of calcium and below that of iron, the even atomic number nuclei are also not very abundant. The highest temperature lines of iron that have been observed are the Lyman-α lines of Fe XXVI at $\sim$1.78 Å. In ionization equilibrium (e.g. Mazzotta *et al* 1998, Bryans *et al* 2009) Fe XXVI has its peak fractional abundance near 100×10^6 K.

From the standpoint of plasma diagnostics, an optically thin spectral line yields three quantities of interest: the total intensity of the line, the profile of the line and the wavelength of the line. The intensities of the lines can be used to calculate electron densities, electron temperatures, element abundances, and can indicate the presence of non-thermal (non-Maxwellian) electrons via line ratios and absolute intensities. The profiles of the lines give information regarding ion temperatures, non-thermal mass motions and multiple plasma flows along the line-of-sight, all via the Doppler effect. The wavelengths give information about bulk plasma flows along the line-of-sight. The diagnostics available to explore different temperature regimes of the solar atmosphere depend on the elements and ions available and where in the UV–x-ray wavelength regions the spectral lines fall.

Plasma diagnostics are a powerful tool in testing models of coronal heating and energy release in flares and other transient activity such as coronal mass ejections (CMEs). However, the solar atmosphere is highly structured and variable in time, and therefore testing models requires plasma diagnostic information at different identifiable positions and times within the structures. These structures are frequently quite small (sub-arcsec; $1'' \simeq 730$ km at the Sun–Earth distance) which requires a spectrometer with high-resolution imaging capability. The ideal plasma diagnostic spectrometer requires imaging such that images of structures can be obtained in individual monochromatic spectral lines. Without the spatial information, plasma diagnostics is only useful in giving average properties of the atmosphere, and is very limited for testing particular theoretical models of atmospheric heating or rapid energy release.

It should be noted that single-line ratios sensitive to either temperature or density give a kind of average value for the plasma within the field-of-view of the observation, even when the spatial resolution is very high. For example, any observation will almost always contain several physically disconnected structures along the line-of-sight with different temperatures/densities. The effect of this on line ratios is discussed for densities by Doschek (1984). Nevertheless, line ratios are a powerful tool for gaining physical insight into solar plasma properties.

In the UV down to about H I Lyman-α ($\sim$1216 Å) aluminium is a highly efficient coating for optics and therefore normal incidence optics can be combined to produce either spatially resolved spectra or monochromatic solar imaging. For example, aluminium plus a thin protective layer of MgF_2-coated optics was used on the S082B slit spectrograph on the *Skylab* manned space station (Bartoe *et al* 1977). If coatings such as SiC or BC are used, the wavelength range can be extended down to about 500 Å, with some loss of efficiency. SiC was used in the solar ultraviolet measurements of emitted radiation (SUMER) spectrometer on the *Solar and Heliospheric Observatory (SOHO)* spacecraft (Wilhelm *et al* 1995). Another approach on *SOHO* was employed in the coronal diagnostic spectrometer (CDS), which used grazing incidence optics and gold coatings for the 150–800 Å spectral range (Harrison *et al* 1995). Below 500 Å multi-layer coatings on normal incidence optics can be used to go deep into the extreme ultraviolet, e.g., instrumentation on the *CORONAS-I, F* spacecraft (e.g. Zhitnik *et al* 1998, 2005) and the *Hinode* spacecraft (Culhane *et al* 2007). The extreme-ultraviolet imaging spectrometer (EIS) on the *Hinode* spacecraft uses SiMo multi-layer coatings on both a mirror and a grating to image two approximately 30–40 Å wavebands near 250 Å and 195 Å (Culhane *et al* 2007). Below about 170 Å and above about 25 Å most solar spectra observations have been made using grazing incidence optics and are quite limited (e.g. see Feldman *et al* (1988) for a review). While the spectra cover large wavelength ranges, the imaging capability is low or even non-existent. Below 25 Å extensive observations have been made using Bragg crystal spectrometers (BCS) (e.g. Doschek 1990). These instruments have obtained outstanding high-resolution solar x-ray spectra, but again the imaging capability is low to zero. There has been some imaging using Bragg crystals as monochromators for a spectral line near the 90° Bragg condition. Some Bragg crystals can be formed into mirrors and at near 90° the incident radiation on the crystal is close to normal incidence and imaging can be achieved without too much astigmatism. So far only the Mg XII line at 8.42 Å has been imaged in this fashion (e.g. Urnov *et al* 2007).

A recent addition to the armada of solar spectrometers flown in orbit is the Extreme Ultraviolet Variability Experiment (EVE, Woods *et al* 2010) launched on the *Solar Dyanmics Observatory* (*SDO*). The prime objective of this instrument is the accurate spectral measurement of solar EUV irradiance. The instrument has relatively low spectral resolution (about 1 Å), but it observes the whole solar disc, covers a very broad wavelength range (50–1050 Å) and has 10 s time resolution. This instrument is important for calibrating other in-orbit

Table 2. High resolution x-ray–UV orbiting spectrometers.

Spacecraft	Instrument	Wavelength range	Reference
Skylab	EUV spectroheliograph S082A	150–350 Å, 300–645 Å	Tousey *et al* (1977)
Skylab	EUV spectrograph S082B	970–3940 Å	Bartoe *et al* (1977)
Skylab	EUV spectroheliometer	280–1340 Å	Reeves *et al* (1977)
OSO-8	UV spectrometer (LPSP)	Six lines between 1000 and 4000 Å	Bonnet *et al* (1978)
OSO-8	UV spectrometer and polarimeter	1170–3600 Å	Bruner (1977)
Hinotori	Rotating Bragg x-ray spectrometers	1.72–1.95 Å, 1.83–1.89 Å	Tanaka (1982)
P78-1	Bragg x-ray spectrometers	Four narrow wavebands between 1.82 and 8.53 Å	Doschek (1983)
P78-1	Bragg x-ray spectrometers	McKenzie *et al* (1980)	
Solar Maximum Mission	Bragg x-ray spectrometers	1.4–22.5 Å	Acton *et al* (1980)
Coronas-I	Spectroheliograph	180–210 Å	Zhitnik *et al* (1998)
Coronas-F	Spectroheliograph (SPIRIT)	280–330 Å	Zhitnik *et al* (2005)
Yohkoh	Bragg x-ray spectrometers	Four bands between 1.76 and 5.11 Å	Culhane *et al* (1991)
SOHO	EUV spectrometer (SUMER)	390–1610 Å	Wilhelm *et al* (1995)
SOHO	EUV spectrometer (CDS)	150–800 Å	Harrison *et al* (1995)
SOHO	UV coronagraph spectrometer (UVCS)	Selected lines, 499–1242 Å	Kohl *et al* (1995)
Hinode	EUV imaging spectrometer (EIS)	170–210 Å, 250–290 Å	Culhane *et al* (2007)

spectrometers and for solar flare observations, as it observes many important flare lines of highly ionized iron. In particular, flare densities can be estimated using a density-sensitive line ratio of Fe XXI lines.

A summary of the most important orbiting high-resolution x-ray–UV spectrometers since and including the *Skylab* manned space station is given in table 2 with references to papers that describe the instruments in detail. These experiments represent a worldwide effort to explore the high-temperature atmosphere of the Sun.

In order to understand the spectroscopic importance of different wavelength regions of the upper solar atmosphere, it is necessary to understand the nature of the solar atmosphere as a function primarily of electron temperature. In the next section we describe and illustrate the complexity of the upper solar atmosphere. We define upper solar atmosphere to be plasma at temperatures between about 2×10^4 and 3×10^6 K. We will treat transient phenomena such as solar flares separately. The temperature range we have chosen extends from what is called the upper chromosphere to temperatures of hot plasma trapped in magnetic flux tubes in so-called coronal active regions.

2. The upper solar atmosphere—morphology

2.1. The photosphere

As noted, the temperature of the white light Sun is about 5500 K in a region called the photosphere. Through about the last third of the solar interior, energy is transported to the surface by both radiation and convection. The convection zone appears in the photosphere as small convective cells called granules (about 1000 km in diameter) that last about 8–20 min before dissipating. In addition, a magnetic dynamo is produced in the convection zone, and magnetic flux erupts through the photosphere in small bundles (about 100 km in diameter) with field strengths of about 1–3 kG. This flux is transported over the photosphere by random gas motions, differential rotation of the Sun (the rotation rate of the Sun is a function of solar latitude) and a meridional flow, which is a general circulation pattern that transports field from the solar equatorial regions towards its poles. The overall result is that the Sun has a general dipole magnetic field with north/south poles, and a complex toroidal component due to the photospheric circulation patterns.

The magnetic field B of the Sun contains energy; the energy density U is $U = B^2/8\pi$. The photospheric flux bundles erupt from below the Sun's surface and become the footpoints of magnetic loops. The motions of these footpoints twist and stress the magnetic field above the photosphere. It is believed by most solar physicists that the twisting and stressing of the field results in a conversion of magnetic to thermal energy which ultimately produces the solar atmosphere (e.g. Parker 1988). The most popular current energy conversion process is believed to be magnetic reconnection. In this process the field lines reconnect to a lower magnetic energy state than the initial state, the difference in energy going into plasma heating, particle acceleration and bulk plasma motions. Wave propagation and dissipation is another popular atmospheric heating mechanism.

2.2. The chromosphere and transition region

Above the photosphere the density of the gas drops abruptly and the gas is heated to temperatures that reach on the order of $1–2 \times 10^4$ K. For this reveiew we define 2×10^4 K as the upper temperature bound of the chromosphere. This region of the Sun is called the chromosphere because the emission of the Balmer line of hydrogen at 6563 Å produces a red ring around the Sun during a total solar eclipse. The chromosphere is composed of small, filamentary and highly dynamic magnetic structures organized into many different appearing forms. The physics of the chromosphere is not well understood and NASA has just selected the Interface Region Imaging Spectrograph (IRIS) Small Explorer Mission to study the physics of the chromosphere in detail at high spatial and spectral resolution. The sizes of chromospheric structures are of the order of a few tenths of an arcsecond (1″ at the solar distance from the

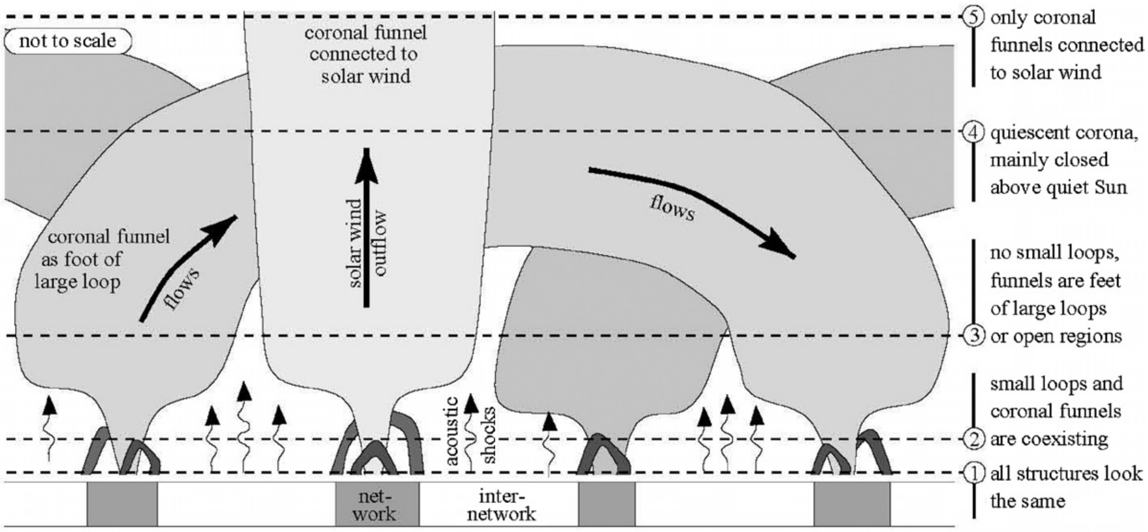

Figure 1. A schematic view of the transition region (from Peter H 2001a *Astron. Astrophys.* **374** 1108 (2001), reproduced with permission © ESO).

Earth is about 725 km) and thus very high spatial resolution is needed.

In the chromosphere the photospheric magnetic field begins to expand (due to the decreasing ratio of gas to magnetic pressure, i.e. the plasma beta) and its direction is not only radial, but horizontal as well. Regions where the field is believed to be mostly horizontal are called magnetic canopies. In the simplest models for heating the atmosphere to temperatures above the upper temperature bound of the chromosphere (which we define as 2×10^4 K), the field is considered to function as a conduit for plasma flow between chromospheric and coronal temperatures. This is the classical model of the solar upper atmosphere (e.g. Gabriel 1976). In this model the near-constancy of the thermal conductive flux from coronal to chromospheric temperatures produces a very thin plasma region with a temperature between about 2×10^4 K and 8×10^5 K. This region that separates the corona from the chromosphere in classical models is called the transition region.

Many observations appear to contradict the classical transition region model (e.g. Feldman 1983, Dowdy *et al* 1986), although with the inclusion of dynamics the model is quite viable (e.g. Judge 2008, Judge and Centeno 2008). A major problem is the lack of sufficient spatial resolution to really resolve the transition region into different temperature region structures (e.g. Vourlidas *et al* 2010). Feldman (1983) called the transition region temperature structures unresolved fine structures (UFSs) while Dowdy *et al* (1986) postulated that they are cool loops, hotter than the chromosphere but cooler than the corona. In these scenarios the transition region is magnetically isolated from the corona. Coronal loops that connect with the chromosphere and have thin transition regions still exist (coronal funnels), but the transition region emission from these thin zones is far weaker than from the observed transition region structures that are magnetically isolated from the corona. Numerical simulations including physics such as wave propagation and radiative transfer are now being developed to explain the many fine-scale features of the chromosphere and transition region, and how these regions of the atmosphere interface with the corona (e.g. Peter *et al* 2006, Hansteen *et al* 2006). These models have so far been successful at explaining many features of the transition region. Figure 1 (from Peter 2001a) shows a schematic summary of the transition region as it now appears from numerous studies, both observational and theoretical.

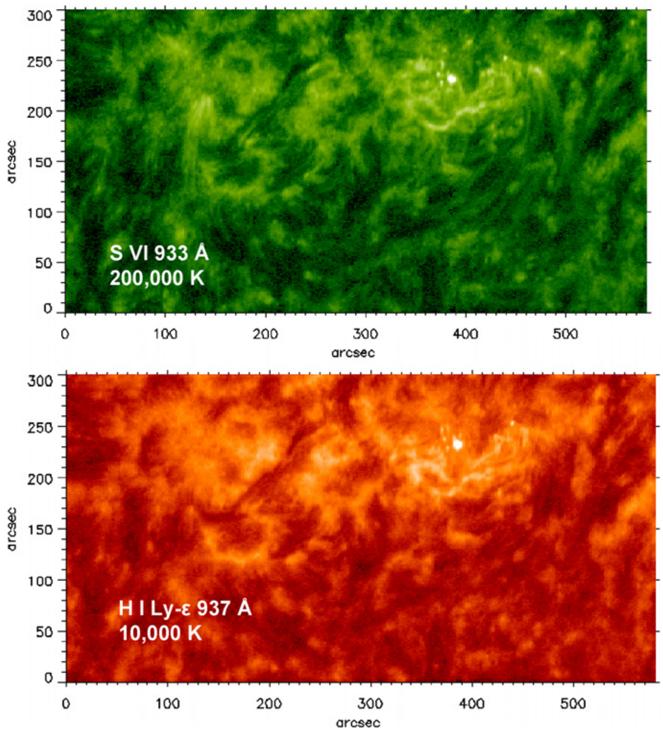

Figure 2. SUMER spectral images of the transition region in lines of H I and S VI.

We do wish to stress that the transition region is currently unresolved spatially. To illustrate this point dramatically, in figure 2 we show a section of the quiet Sun in spectral lines of H I Lyman-ϵ and S VI obtained from SUMER. Note that the

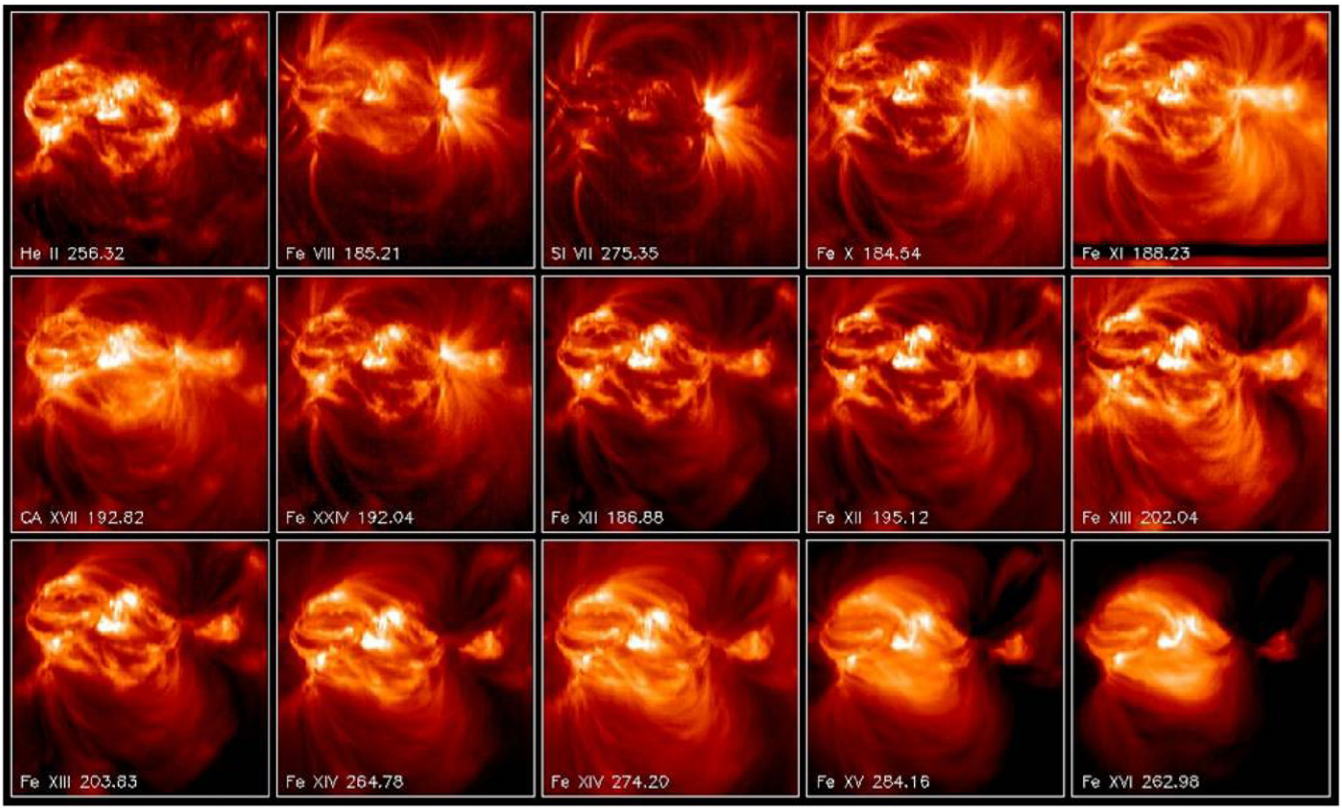

Figure 3. An active region as seen in monochromatic images recorded in different spectral lines of the upper transition region and coronal ions. The images were generated in raster mode by *Hinode*/EIS. Note the many loop-like structures.

structures in both images look extremely similar, even though the two lines are formed at much different temperatures. Since plasma at two different temperatures cannot occupy the same volume, it is clear that the differences between the emission in the two spectral images are below the resolving power of SUMER, which is currently about 1400 km, or 2″.

2.3. The corona

Above about 8×10^5 K the plasma is considered to be part of the solar corona, the pearly white halo that surrounds the Sun during a total solar eclipse. This halo emission is due to Thomson scattering of visible disc radiation from the Sun by free electrons in what is considered a fully ionized coronal plasma. The connection between the corona and the chromosphere/transition region is not understood at present, principally because (in the opinion of the authors) the spatial resolution in the corona and transition region is not sufficiently high to connect structures seen in the corona decisively to the lower temperature transition region and chromospheric structures. The highest spatial resolution yet achieved in the corona is 1″, but a few tenths of an arcsec is believed to be needed to interface properly dynamical coronal phenomena with lower temperature dynamical phenomena. Another problem is that no presently operating space imaging spectrometer or imager has complete temperature coverage from the chromosphere/transition region into the corona. Thus, phenomena can escape observation by heating or cooling into temperature regions for which the observing instrument is not sensitive.

The basic coronal structure appears as a loop (i.e. plasma confined to a magnetic flux tube), and as temperatures increase from about 1×10^6 K to about 3×10^6 K the appearance of loops becomes more amorphous. The corona is bright and produces a bewildering array of loop and loop-like structures in active regions. Active regions are upper atmosphere areas over regions of the photosphere with enhanced magnetic field strengths. In particular sunspots, cooler areas of the photosphere, have very strong magnetic fields and coronal emission in active regions with complex sunspot activity in the photosphere is very strong and this is also where dynamical events such as solar flares occur. Figure 3 shows an active region seen in an image recorded in radiation from lines of a different upper transition region and coronal ions obtained from the EIS spectrometer on *Hinode*.

The heating of plasma in coronal loops is currently a hot topic in solar physics. A popular model is the nanoflare model (Patsourakos and Klimchuk 2006, Dahlburg *et al* 2009), where small flare-like reconnection events occur in sub-resolution magnetic field strands in loops. Another current idea under investigation is that dynamical events in the chromosphere propagate into the corona and thereby supply the heating (De Pontieu *et al* 2009). The test of these models depends critically on spectroscopic observations. In the nanoflare model, small amounts of loop plasma are heated to temperatures of about 1×10^7 K and therefore weak emission should be seen in a spectral line formed near this temperature. This weak emission

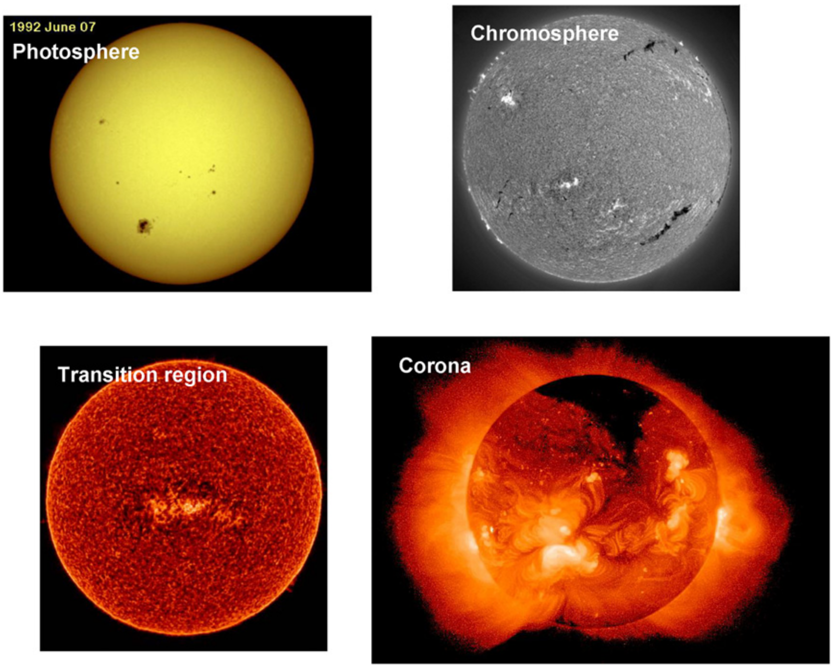

Figure 4. Images of the Sun illustrating the principal regions of the upper solar atmosphere. The images were recorded on different days and at different times. The transition region image was recorded by SUMER in a spectral line of S VI (933, Å), and the coronal image was recorded by the soft x-ray telescope on the *Yohkoh* spacecraft.

has in fact been seen in some cases (Shestov *et al* 2010). In the chromospheric heating model, plasma flowing into loops from the chromosphere should produce a significant Doppler signature on spectral lines emitted from loop plasmas (e.g. Peter 2001b). Testing these models is currently underway.

Figure 4 summarizes the morphology of the upper solar atmosphere in photospheric, chromospheric, transition regions, and coronal radiation. The four images were recorded on different days. Note that the white light image appears featureless except for sunspots although a higher resolution/contrast image would show the granules. The chromosphere and transition region images show very small structures covering the entire disc. The coronal image shows larger-appearing structures, reflecting the expansion of the magnetic field as the plasma β decreases. (The plasma β is the ratio of thermal to magnetic pressure.) However, recent results indicate that the corona is also composed of structures not yet resolved by current instrumentation. These sub-resolution structures reside within the larger loop-like envelops.

2.4. Solar activity

Solar activity takes many forms, from prominences, cool material suspended by magnetic fields in the corona, to solar flares and CMEs. Solar flares are relatively small areas of the solar atmosphere (from a few square arcsec to a few square arcmin) where coronal plasma is produced that can reach temperatures on the order of 20–40 $\times$ 10^6 K and electron densities of about 10^{11}–10^{13} cm^{-3}. There is concurrent emission in the UV, radio, soft x-rays, hard x-rays ($\leqslant$1 Å), and sometimes even white light. Figure 5 shows a typical signature of a flare in various radiations. The figure also shows the model (the so-called standard model) where flares are believed to occur as a result of magnetic reconnection in the corona. In this model, reconnection heats plasma and accelerates high-energy particles. In the model some of these particles as well as a thermal conduction front move down the flux lines into the chromosphere where they heat the gas that flows upwards (chromospheric evaporation) into reconnected closed flux tubes (loops) producing the high coronal densities and multimillion degree soft x-ray emitting plasma (e.g. Reeves *et al* 2007). Also shown in figure 5 is an image of a flare above the limb seen mostly in a spectral line of Ca XVII (about 5×10^6 K) recorded by *Hinode*/EIS. This feature is actually a blend of Ca XVII, Fe XI (about 1.4×10^6 K) and O V (about 2×10^5 K) (see Ko *et al* (2009)), but in the flare image it is mostly Ca XVII, especially at the top of the loop structures. One of the continuing research goals using EIS is to investigate the plasma conditions in the region above the bright diamond ring-like area in the image where reconnection is supposed to occur in the standard model.

CMEs are thought by some to occur as a result of the same reconnection that produces flares and in this scenario are the result of the reconnection process above the reconnection region, in contrast to the flare just described that occurs below the reconnection region. The CME is an outward propagating flux rope into the corona that becomes enormous in size (see figure 6). The CME shocks the corona above it and piles up plasma into an outward propagating front. A reasonably accurate layman description of a CME is that it is a billion tons of gas moving at a speed of about a million miles an hour. Behind this front there is often cool plasma at prominence temperatures. Some CMEs can be observed all the way to the Earth. CMEs can shock interplanetary gas and produce solar energetic particles (SEPs) that are the worst culprits of space weather effects at the Earth.

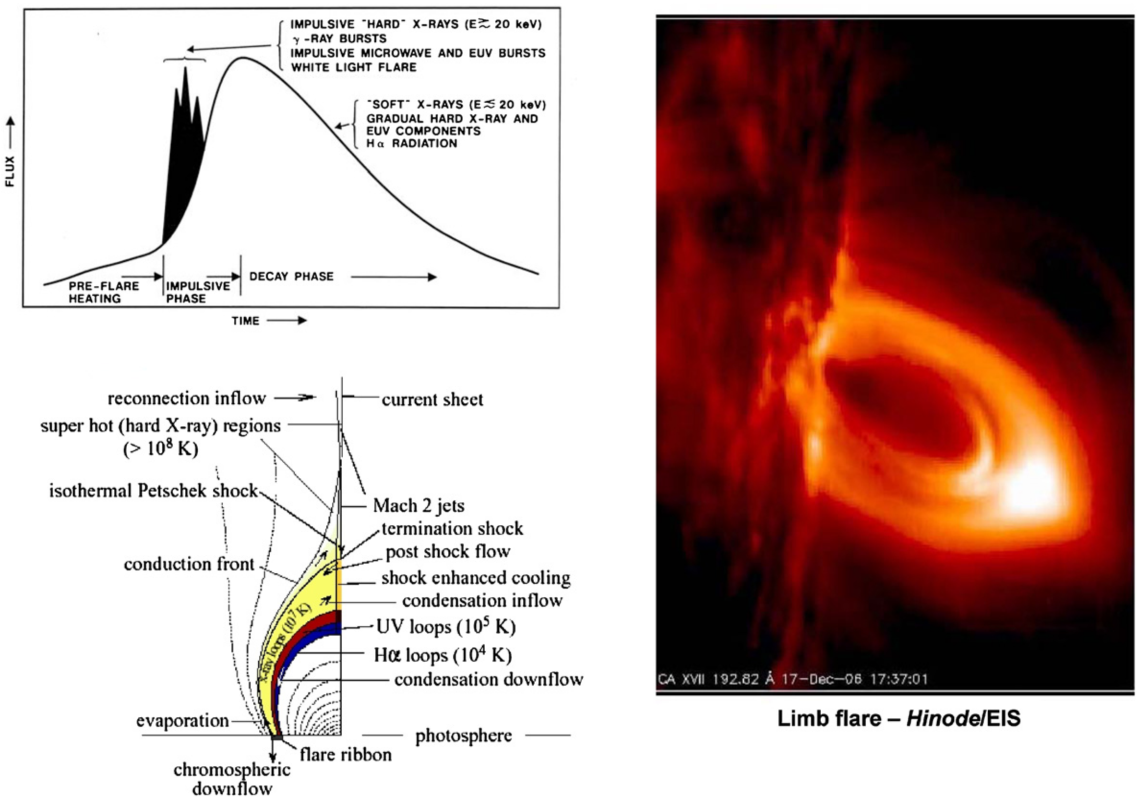

Figure 5. A typical solar flare light in radiation of different wavelengths, a schematic of the standard model of a solar flare and an image of a solar limb flare recorded by *Hinode*/EIS.

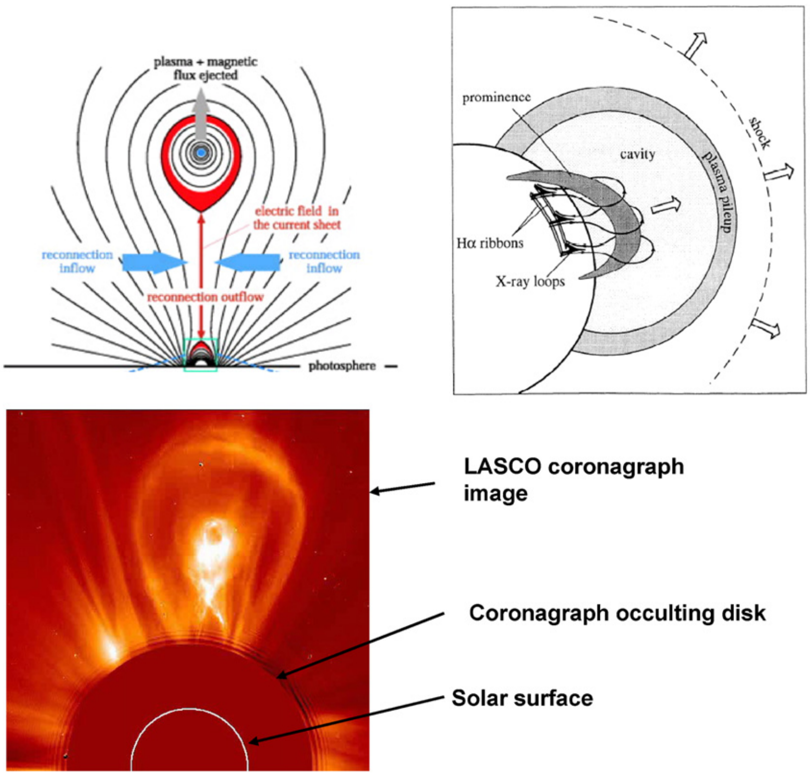

Figure 6. Left panel: schematic of CME formation. Right panel: three-dimensional representation of an expanding CME and associated plasma. Bottom left: a white light image from the LASCO coronagraph on *SOHO*. The CME actually was ejected in the east–west direction. It has been rotated for ease in comparing with the top left panel.

There are many observational difficulties with the standard model described above. As an example, there can be a CME without any detectable signature below the postulated reconnection region on the solar disc (Robbrecht *et al* 2009).

3. Spectroscopy: the transition region

We define the transition region to be that region of the atmosphere between $\sim 2 \times 10^4$ and 8×10^5 K. Useful spectral lines for this region occur throughout a spectral range that extends from roughly 550 Å (O IV) up to 2000 Å. Table 3 shows a list of many major solar spectral lines up to flare temperatures useful for various diagnostic purposes. The temperatures of maximum ionization equilibrium are also shown. (A list of forbidden lines in the 500–1500 Å wavelength range, many of which are useful above the solar limb, is published by Feldman and Doschek (2007).) There are several sets of spectral lines that have proven useful for diagnosing the lower transition region. Strong lines such as the 1550 Å C IV doublet have been used to diagnose transient transition region phenomena, such as explosive events (e.g. Brueckner and Bartoe 1983). Explosive events are transient phenomena that occur over small spatial areas ($\leqslant$1000 km) and last for a few tens of minutes and can produce upflowing plasma up to 400 km s^{-1}.

The temperatures in table 3 should be regarded as only a guide to the temperature of emission. In reality, the maximum temperature of emission is the product of the excitation rate coefficient and the fractional ion number density called the contribution function. This temperature varies with wavelength but can also be misleading. Figure 7 shows contribution functions for lines of O IV and O VI. In the O IV case, the two curves have different maximum temperatures, but in the O VI case the two maximum temperatures are about the same. However, the ratio of the two O VI lines is clearly a function of temperature. Readers are cautioned to work with the full contribution functions for a detailed understanding of the temperature behaviour of the lines in table 3.

Figure 8 shows a single C IV SUMER spectrum oriented in the solar north–south direction. The spectrum is stigmatic along the slit with a pixel size of 1″. At the position of the arrow note the strongly blueshifted blob-like appearing structure. Phenomena such as this are possibly due to magnetic reconnection (e.g. Innes *et al* 1997). The SUMER spectrum is part of a raster, and the contour to the left of the spectrum in the figure shows the spatial extent of the upflow, obtained from the raster image, which has a maximum speed of about 30 km s^{-1}. The chromosphere and lower transition region are the sites of most of the dramatic transient phenomena that exhibit large upflows or downflows and/or large turbulence or non-thermal motions (measured from line profiles). For example, in addition to explosive events short-lived transient transition region phenomena known as blinkers have also been studied (e.g. Harrison 1997, Harrison *et al* 2003). These events were discovered using CDS spectra. The corona around 10^6 K is in comparison quite quiet, generally showing no large turbulent motions or directed plasma flows, or extended emission wings on spectral lines that might indicate jets from reconnection that is postulated to occur in the corona (e.g. Parker 1988). Spectra such as shown in figure 8 give information on the energetics of transient events from which quantities such as mass and energy input into the corona can be calculated. Some other good spectral lines for this kind of work are C III 977 Å, N V 1238, 1242 Å, and Si IV 1393, 1402 Å.

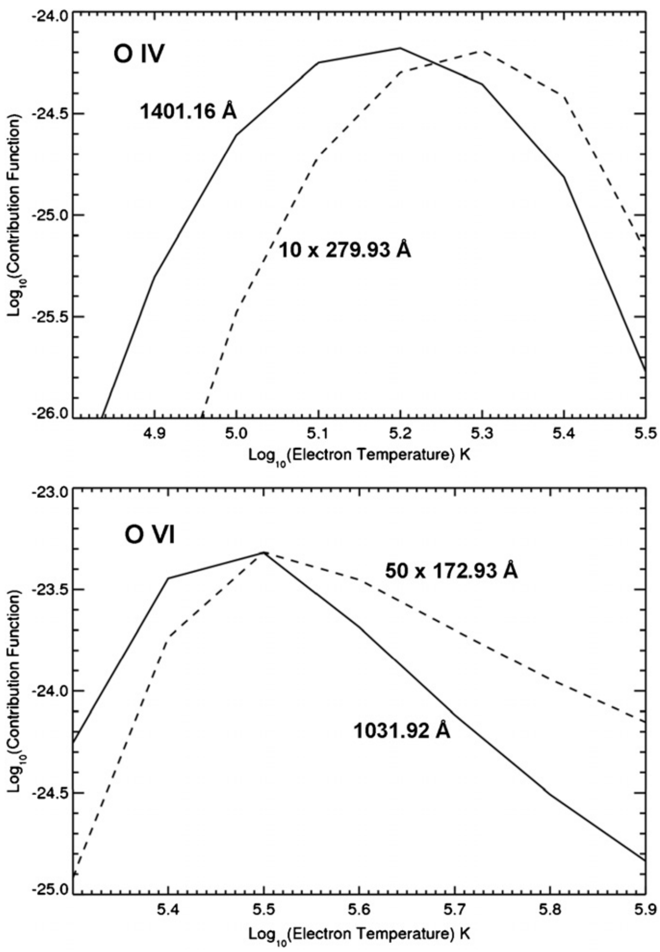

Figure 7. Contribution functions (cm^3 s^{-1} sr^{-1}), i.e. line intensities per unit emission measure. A nominal electron density of 2×10^9 cm^{-3} was used in order to illustrate the line temperature dependences.

The transition region lines have also been used to study plasma flows in loops. As mentioned, loop-like structures are the dominant structures in the solar atmosphere. Typically, the line profiles in a rastered region of the solar disc are fit with Gaussian line profiles and their intensities, widths and centroids are determined. No solar instruments to date have had absolute wavelength calibrating sources, and therefore a decision must be made as to what are the rest wavelengths of the spectral lines being used. This is often done by making an assumption, e.g., the chromosphere is stationary on average, or a quiet Sun coronal region exhibits no net flow on average. It is desirable that an absolute wavelength capability be part of a future spectroscopy experiment. For best results an on-board calibration lamp would be desirable, but this is presently very difficult to implement at EUV wavebands.

Table 3. Important solar UV–x-ray spectral lines.

Ion	Wavelengths (Å)	$10^{-6} \times$ Temperature (K)
H I Lyα	1215.64 and H I Lyman series	0.01
He I	584.32	0.02
He II	256.32, 303.78 and 1640 multiplet	0.1
C II	1036.34, 1037.02, 1334.53, 1335.66, 1335.71	0.022
C III	977.02, 1176 multiplet, 1247.38, 1906.68, 1908.73	0.071
C IV	1548.20, 1550.77	0.1
N III	685, 990 and 1750 multiplets	0.079
N IV	765.15, 1483.32, 1486.50	0.14
N V	1238.82, 1242.80	0.2
O I	1302.16, 1304.86, 1306.03	0.01
O II	835 multiplet	0.045
O III	703 and 835 multiplets, 1660.81, 1666.15	0.089
O IV	279.93, 554, 788 and 1401 multiplets	0.16
O V	629.73, 760 multiplet, 1213.81, 1218.34, 1371.29	0.25
O VI	172.93, 173.08, 183.94, 184.12, 1031.92, 1037.61	0.32
O VII	21.60, 1623.63	1.0
O VIII	18.97	2.5
Ne VI	401, 560 and 1000 multiplets	0.40
Ne VII	465.22, 895.18	0.50
Ne VIII	770.41, 780.32	0.63
Ne IX	13.45, 1248.08	2.0
Ne X	12.13	4.5
Mg VI	401 multiplet, 1190.07, 1191.64, 1805.97, 1806.5	0.45
Mg VII	434 multiplet, 868.11	0.63
Mg VIII	315 multiplet, 430.47, 436.73, 772.28	0.79
Mg IX	368.07, 705.72	1.0
Mg X	609.79, 624.97	1.1
Mg XI	9.17, 997.44	4.0
Mg XII	8.42	7.9
Al III	1854.72, 1862.79	0.04
Si II	1304.37, 1526.71, 1533.43, 1808.01, 1816.93	0.016
Si III	1206.51, 1294 multiplet, 1892.03	0.032
Si IV	457.82, 458.16, 1122 multiplet, 1393.76, 1402.77	0.063
Si VI	246.00, 249.12	0.35
Si VII	275 multiplet, 1049.22	0.63
Si VIII	314.31, 316.20, 319.83, 944.38, 949.22, 1440.49, 1445.76	0.79
Si IX	223, 290 and 345 multiplets, 694.70, 950.14	1.0
Si X	253 and 272 multiplets, 347.42, 356.05, 638.94	1.3
Si XI	303.318, 580.85	1.6
Si XII	499.41, 520.67	2.0
Si XIII	6.65, 814.72	6.3
Si XIV	6.18	13.0
S II	1253.79, 1259.53	0.02
S III	1015 and 1193 multiplets	0.050
S IV	750 multiplet, 809.67, 815.95, 1062.66, 1072.99	0.11
S V	786.48, 1204.30	0.16
S VI	933.38, 944.52	0.20
S VIII	198.55, 202.60	0.79
S IX	225 multiplet	1.0
S X	257.16, 259.52, 264.24, 1196.26, 1213.00	1.3
S XI	186, 291 and 242 multiplets	1.8
S XII	215 multiplet, 227.48, 234.48, 288.45, 299.50	2.0
S XIII	256.66, 491.44	2.5
S XIV	417.61, 445.77	3.2
S XV	5.04	10.0
S XVI	4.73	20.0
Ar VII	585.75, 885.55	0.32
Ar VIII	700.24, 713.81	0.40
Ar XI	188 multiplet, 1392.12	1.6
Ar XII	215.49, 218.29, 224.25, 1018.79, 1054.59	2.0
Ar XIII	205 and 242 multiplets	2.5
Ar XIV	188 and 257 multiplets	3.2
Ar XV	221.15, 424.01	3.5
Ar XVI	353.92, 389.14	4.0

Table 3. (Continued.)

Ion	Wavelengths (Å)	10^{-6} × Temperature (K)
Ar XVII	3.95	13.0
Ar XVIII	3.73	28.0
Ca XIII	163 multiplet, 1133.76	2.5
Ca XIV	183.46, 186.61, 193.87, 1291.61	3.2
Ca XV	177 and 210 multiplets, 1375.96	4.0
Ca XVI	208.59, 224.55	4.2
Ca XVII	192.86, 371.04	5.0
Ca XVIII	302.21, 344.77	6.3
Ca XIX	3.177	18.0
Ca XX	3.02	45.0
Fe VIII	185.21, 186.60	0.63
Fe IX	171.08, 241.74, 244.91	1.0
Fe X	Many lines between 170 and 230, 1028.02, 1463.49	1.1
Fe XI	Many lines between 180 and 370, 1467.08	1.3
Fe XII	192.39, 193.51, 195.12, 364 multiplet, 1242.00, 1349.40	1.4
Fe XIII	Many lines between 200 and 370	1.6
Fe XIV	219.14, 264 multiplet, 274.20, 334.18, 353.84	1.8
Fe XV	284.15, 417.24	2.0
Fe XVI	251.06, 262.97, 335.41, 360.80	2.2
Fe XVII	10–20 and 254.87, 1153.16	3.2
Fe XVIII	10–20 and 93.93, 103.95	5.0
Fe XIX through Fe XXII	10–20 and 90–140	6.3–10.0
Fe XXIII	8–15 and 132.85, 263.76	13.0
Fe XXIV	8–15 and 192.02, 255.09	16.0
Fe XXV	1.85	50.0
Fe XXVI	1.78	112.0

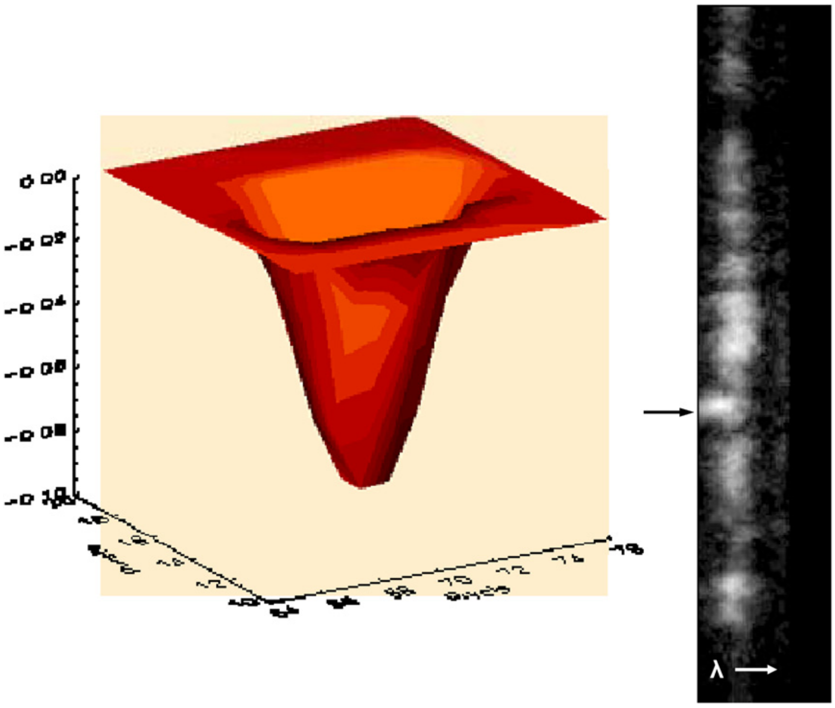

Figure 8. Right: a single SUMER spectrum showing an explosive event. Left: a Doppler shift contour from the rastered image that shows the spatial extent of the explosive event.

Figure 9 shows part of an active region raster that contains plume-like outflow regions apparent in the Ne VIII doublet lines at 770 and 780 Å (upper transition region, 6.3×10^5 K). For this observation the 770 Å line was observed in second order, near the lower transition region C IV 1550 Å doublet (1×10^5 K) and a second order S V line (786.48 Å). The left-hand panels show raster images of the Ne VIII and S V line intensities. The right-hand panels show raster images of the centroids of these lines, with the Ne VIII intensity contours overlaid onto the centroid images. In the centroid images, blue represents a Doppler motion towards the observer (upflow) and red represents a Doppler downflow. The pale blue areas are

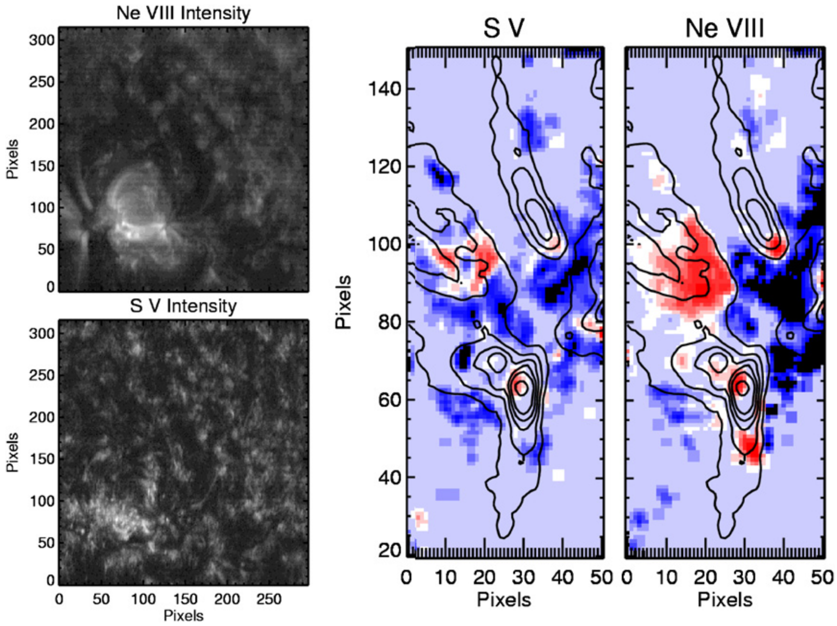

Figure 9. Left panels: SUMER active region raster images in lines of Ne VIII and S V. Right panels: centroid images in Ne VIII and S V overlaid with Ne VIII intensity contours. The centroid maps only cover the active region fan-like loop structures seen in the lower left corner of the Ne VIII image (from Doschek 2006).

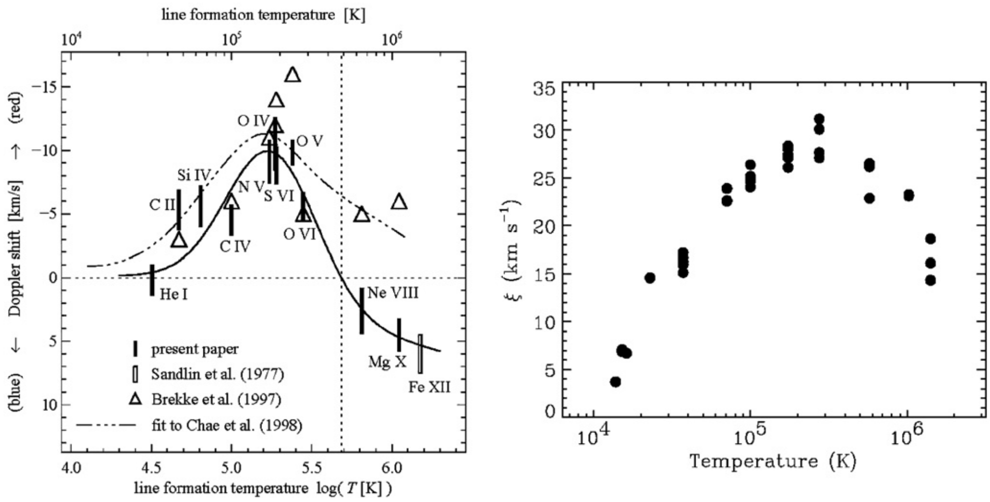

Figure 10. Left panel: average net radial flow in the quiet Sun as a function of electron temperature from SUMER data (positive = downflow (from Peter H and Judge P G 1999 *Astrophys. J.* **522** 1148). Right panel: average quiet Sun non-thermal motion as a function of electron temperature (from Chae J *et al* 1998b *Astrophys. J.* **505** 957).

regions where the intensities of one or both of the lines are too weak for a meaningful measurement. The S V and Ne VIII centroid images show a downflow at the bases of the plume-like structures. Many studies of this sort have been made (e.g. Winebarger *et al* 2002, Marsch *et al* 2004, Doschek 2006). The principal objective of this type of work is to investigate the dynamics of coronal loops as a tool for understanding and testing theories of coronal heating. Numerical simulations of loops assuming different heating mechanisms are coupled to atomic data bases to predict spectral line behaviour for comparison with observations.

We now discuss some aspects of transition region lines that are also common to lines formed at coronal temperatures. If centroid images of the transition region are made, it is best to determine the wavelength of the transition region line by assuming that the chromosphere is on average stationary, and then finding from instrument characteristics the wavelength of the transition region line. This wavelength can be compared with a laboratory wavelength and in this manner upflows and downflows can be determined. When this is done for spectral lines formed over a range of temperatures, it is found that there are small net average downflows in the atmosphere, which vary systematically as a function of temperature (e.g. Doschek *et al* 1976, Chae *et al* 1998a, Peter and Judge 1999). The net redshifts/downflows are illustrated in figure 10. As can be seen, the peak downflow is near 10^5 K and is of the order of

12 km s^{-1}. This downflow speed in Doppler shift is actually smaller than the net line width, assuming a Gaussian profile which is approximately correct for lower transition region lines. It is therefore possible that there is no net downflow, i.e. the downflowing material may be denser than the upflowing material which would make the downflowing material brighter and cause a net redshift. However, the total mass flow may be zero in this circumstance. A convincing explanation for the redshifts has yet to be found although recent modelling may provide an explanation (V Hansteen, private communication).

In addition to downflows, spectral lines in all regions of the solar atmosphere are wider than expected from pure Doppler thermal broadening in ionization equilibrium, and the excess width is usually interpreted as a non-thermal broadening. It may be turbulence, but this is unclear. It could simply be random bulk motions of many elements of spatially unresolved structures. At the densities typically encountered in the solar atmosphere the plasma should be close to ionization equilibrium or achieve it very quickly. There are models that predict non-equilibrium effects, e.g., flows through a steep temperature gradient, but no one has yet conclusively demonstrated a non-ionization equilibrium effect to our knowledge.

The non-thermal speeds are deconvolved from the thermal Doppler and instrument broadenings by assuming that all broadening mechanisms produce Gaussian line profiles. In this case, the convolved line profile is also a Gaussian with a full width at half maximum (FWHM) intensity that is the sum of the squares of the FWHMs of the three broadening components. As with the downflows, the deconvolved non-thermal motions are also found on average to be a function of electron temperature, as shown in figure 10 (from Chae *et al* (1998b)). To give the reader an idea of the size of the non-thermal speeds compared to the thermal Doppler speeds, at 1×10^5 K the thermal Doppler speed for C IV is about 12 km s^{-1}. At 1.4×10^6 K the thermal Doppler speed for Fe XII is about 20 km s^{-1}.

The origin of the non-thermal motions is presently unknown. Interpretations have been made assuming that the motions are due to the propagation of waves through the atmosphere (e.g. Bruner and McWhirter 1979), and/or broadening due to relative motions of UFS. Whatever theory is invoked to explain the motions must account for their temperature dependence. The theory must also account for the fact that the motions vary in different structures, and in fact go to about zero in some regions of quiescent prominences (Feldman and Doschek 1977). They appear to be related to magnetic field strength and morphology of the structure.

Figure 10 shows that the peak of the non-thermal motions is also close to 10^5 K and is of the order of 30 km s^{-1}. A good conclusion seems to be that the downflows and non-thermal widths of spectral lines formed in the transition region and corona will be an important test of any theory developed to explain coronal heating and the propagation of energy from the chromosphere into the corona.

The transition region lines provide some excellent electron density diagnostics. Knowing the electron density is extremely important because the radiative losses of a plasma are proportional to the density squared. Theories of loop heating depend critically on knowing the density. Densities are found from the intensity ratios of lines, one of which involves a metastable level. Because of the metastable level, the mixing of electron impact collisions and spontaneous radiative decay produces density sensitive line ratios (see Phillips *et al* (2008)). By now many of the important density diagnostic line ratios have been thoroughly investigated. Solar physicists routinely use the CHIANTI atomic data base (e.g. Dere *et al* 2009) to determine densities (and other diagnostic properties as well).

An example of lower transition region density diagnostics using C III lines is shown in figure 11. The best C III density diagnostic is the 1175.987/1175.263 ratio because the lines are close in wavelength and therefore instrumental sensitivity as a function of wavelength is not an issue. Also, there is no temperature sensitivity in the line ratio. However, the ratio is not too sensitive; it is best for densities between about 10^8 and 10^9 cm^{-3}. The 1175/977 ratio is good between about 10^9 and 10^{10} cm^{-3}, but there is also some temperature sensitivity. SUMER can observe both lines but not simultaneously. The 1247/1909 and 1909/977 ratios are complicated because they are both temperature and density sensitive. The 1909 Å line is not available with SUMER but was observed using the NRL S082B slit spectrograph on *Skylab*.

Another lower transition region multiplet with density sensitivity is the O IV intersystem multiplet near 1400 Å (see figure 12). The best diagnostic is the 1407/1404 ratio, but the 1404 line is blended with an intersystem line of S IV. The S IV blend can be approximately removed if the 1406 S IV line is also observed (see figure 13). The upper left panel shows three O IV spectra recorded on film by the NRL S082-B slit spectrograph on *Skylab*. The leftmost spectrum is a quiet Sun spectrum. Spectra (b) and (c) are from flaring regions. Note that the line designated as 1405 (the 1404 line) is stronger than the 1407 line in the quiet Sun spectrum, but has equal intensity to the 1407 line in the flare spectra (equal photographic densities imply equal intensities). In the flare spectra the 1404/1407 ratio of unity implies from the lower left panel a density of about 3×10^{10} cm^{-3}. From figure 13 this density implies a 1404/1406 ratio of 0.2. Because the 1406 S IV line also has the same intensity as the 1404 and 1407 O IV lines in the flare spectra, this means that the true unblended 1404/1407 ratio is about 0.8 rather than unity. This reduces the density only a little, to about 2×10^{10} cm^{-3}. These transition region diagnostics have yet to be applied to many flare spectra because the spectrometers available up to now have had severe limitations for flares regarding data rates, sensitivity and time resolution, i.e. the spectrometers were not optimized for rapidly evolving transient phenomena.

The right-hand panels in figure 12 show ratios proportional to density and temperature (top panel) and to primarily temperature (bottom panel). It is also important to have temperature sensitive line ratios, in order to check the validity of ionization equilibrium and to search for non-thermal particles (see section 4). Unfortunately, most temperature-sensitive line ratios are formed by using spectral lines with large wavelength differences, i.e. the electron impact excitation

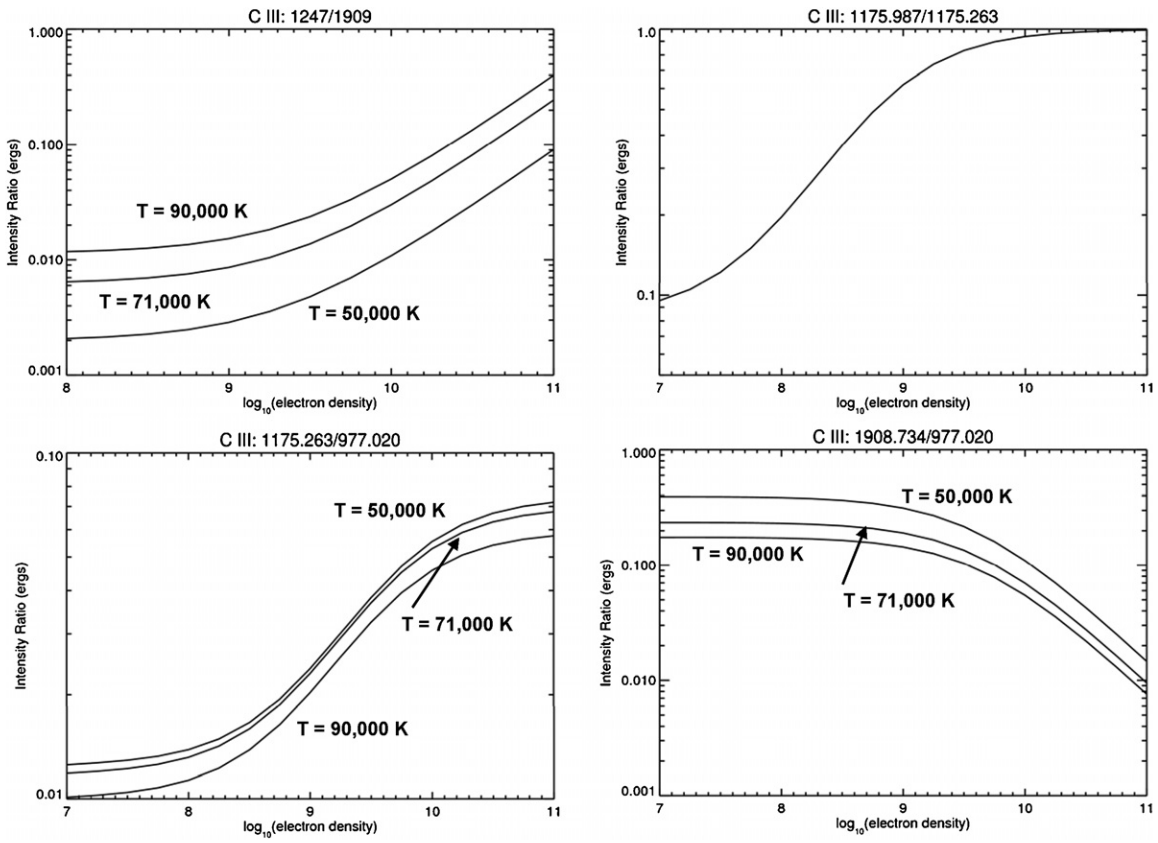

Figure 11. Diagnostic line ratios for C III (from CHIANTI).

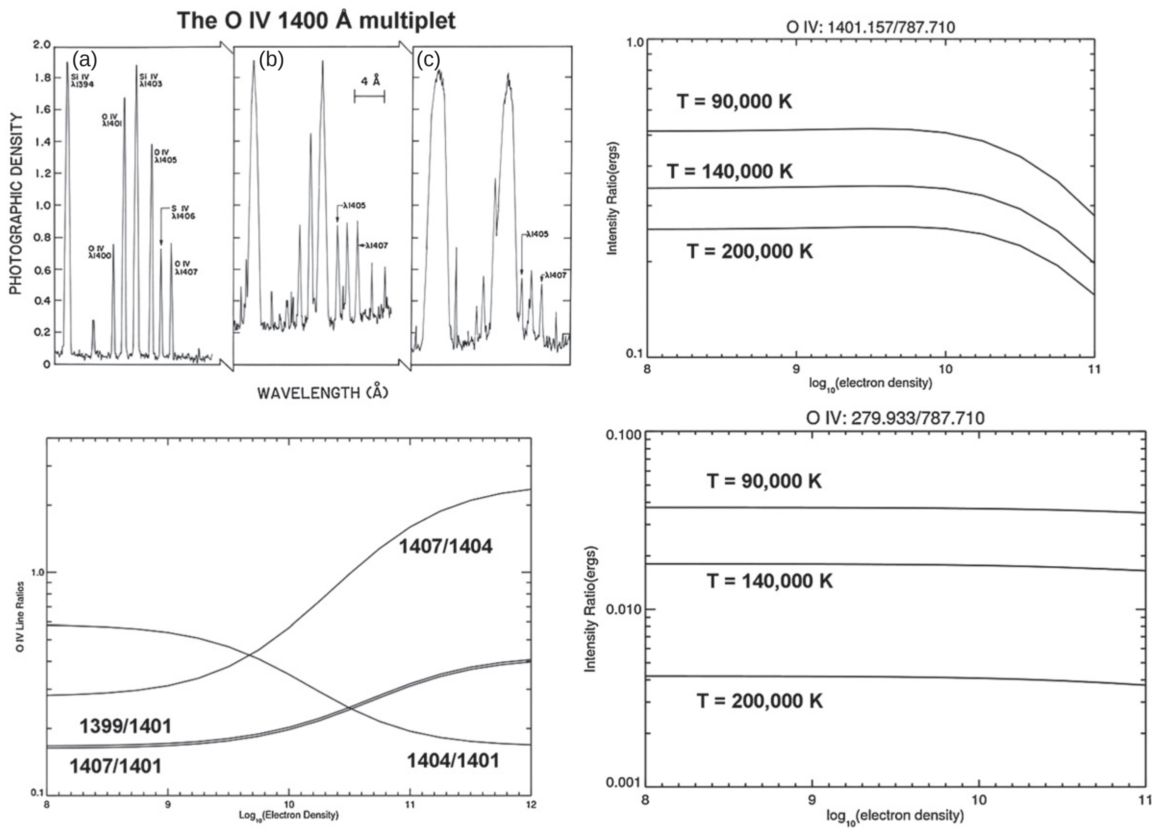

Figure 12. Diagnostic line ratios for O IV (from CHIANTI).

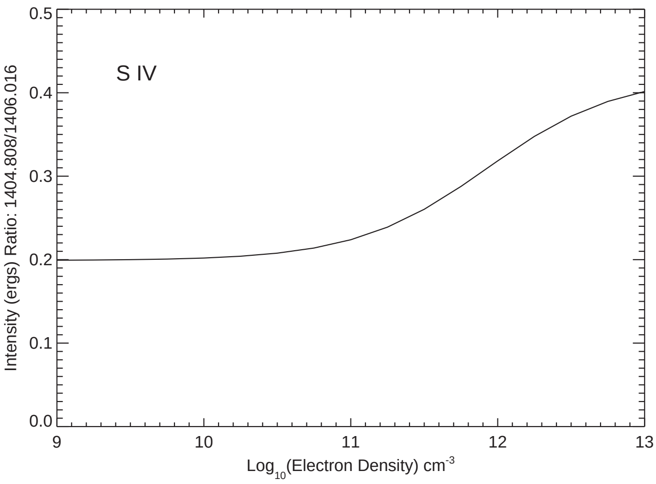

Figure 13. Diagnostic line ratios for S IV (from CHIANTI).

into one of the levels must require an energy comparable to the thermal energy in order to have a good temperature diagnostic. That is, one line samples the bulk of the electron population, while the other line samples primarily the high-energy part of the population. The 279/787 ratio shown in the lower right panel has been used to measure temperatures in quiet Sun regions (Muglach *et al* 2010). Unfortunately the results do not support ionization equilibrium! The derived temperatures are too high for reasons that are presently unknown. This result needs further investigation and confirmation.

In summary, excellent diagnostic spectral lines for the transition region can be found between about 300 and 2000 Å. Between about 1200 and 2000 Å, only the lower transition region ($T \leqslant 2.5 \times 10^5$ K) produces useful diagnostics. The upper transition region ($T \leqslant 1 \times 10^6$ K) is well represented in the 500–1200 Å range and strong lower transition region lines reappear at the short end of this range and a little below due to transitions involving a change in principal quantum number (e.g. 629 Å O V).

4. Spectroscopy: the corona

We define the corona as the temperature region above about 0.8–1×10^6 K. In this regime the principal structures that can be defined have loop or loop-segment structures. In active regions the footpoints of these loops have the appearance of spot-like structures at around 1×10^6 K. Groups of these structures are termed moss from the analysis of TRACE images (Berger *et al* 1999). It was first demonstrated by Fletcher and De Pontieu (1999) using CDS spectra that the moss represents the footpoints of hot loops. Analysis of EUV coronal lines has taught us much about the physical properties of the corona.

For example, analysis of spectra obtained by SUMER and EIS above the solar limb have revealed a remarkable result. In the quiet Sun the temperature is isothermal to within the accuracy of the atomic data at a temperature of about 1.4×10^6 K (e.g. Feldman *et al* 1999, Warren and Warshall 2002). This temperature represents the average temperature of unresolved loops and perhaps background emission along lines-of-sight above the limb. This result is obtained in the following way.

The intensity of a spectral line is proportional to the so-called emission measure, which is the square of the electron density times either the volume of the plasma emitting the line or the line-of-sight distance through the plasma, depending on how the intensity is defined. The proportionality function depends on the element abundance, the ionization fraction of the ion and the rate at which the atomic transition can be excited. The latter two quantities depend on temperature and electron density. For example, the equation for the intensity $\mathrm{d}I^k_{j,i}$ of line k from a small volume element $\mathrm{d}V$ can be written as

$$\mathrm{d}I^k_{j,i} = h\nu_{j,i} A_Z N^k_j(T_e, N_e) A_{j,i}\, \mathrm{d}V, \tag{2}$$

where $h\nu_{j,i}$ is the transition energy, A_Z is the element abundance (Z is the atomic number), $A_{j,i}$ is the spontaneous decay rate from level j to level i and N^k_j is the number density of the upper level j. The quantity N^k_j is calculated by detailed balancing of all the collisional and radiative processes in as many levels of the ion as is necessary to get a converged result. The detailed balancing depends on the excitation rate coefficients (cm^3 s^{-1}) due to all the electron (and sometimes proton) impact excitations as well as on all the possible radiative decay routes. The value of N^k_j also depends on the ionization fraction. The result is that the intensity can be written as

$$I^k_{j,i} = \int f_k(T_e, N_e, A_Z) N_e^2\, \mathrm{d}V, \tag{3}$$

where N_e is the electron density, f_k is a proportionality function that contains the product of the ion density calculated from the ionization balance times the excitation rate coefficient for the line and V is the volume in which the spectral line is emitted and the product $N_e^2 V$ is the volume emission measure.

The emission measure as a function of temperature can be found by inverting the integral equation above using many lines formed at different temperatures in ionization equilibrium (e.g. see Phillips *et al* (2008)). This assumes that ionization equilibrium is valid and if lines of different elements are used, then the relative abundances of the elements must be known. The actual inversion must be done carefully as the problem is not well conditioned.

However, in the special case where the plasma is isothermal at temperature T_e, the equation above reduces to

$$I^k_{j,i}(\text{isothermal}) = f_k(T_e, N_e, A_Z) N_e^2 V. \tag{4}$$

In this case, the emission measure is the intensity divided by the proportionality function f_k. The emission measure plotted as a function of temperature for a particular spectral line k looks roughly like a parabolic curve with a minimum that occurs where the product of the ion fraction and excitation rate is largest. Any point on the curve defines a temperature and emission measure that is consistent with the measured intensity of the line in ionization equilibrium. If one plots these curves on a single graph for many lines formed over a range of coronal temperatures and finds that there is a common

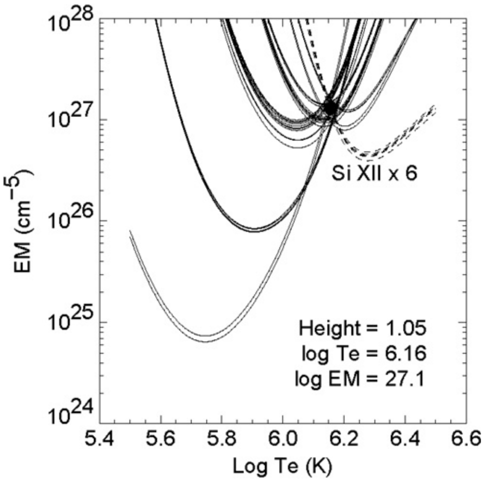

Figure 14. Determination (see the text) of the quiet Sun electron temperature above the limb from SUMER spectra and a range of spectral lines from Si ions (from Warren H P and Warshall A D 2002 *Astrophys. J.* **571** 999).

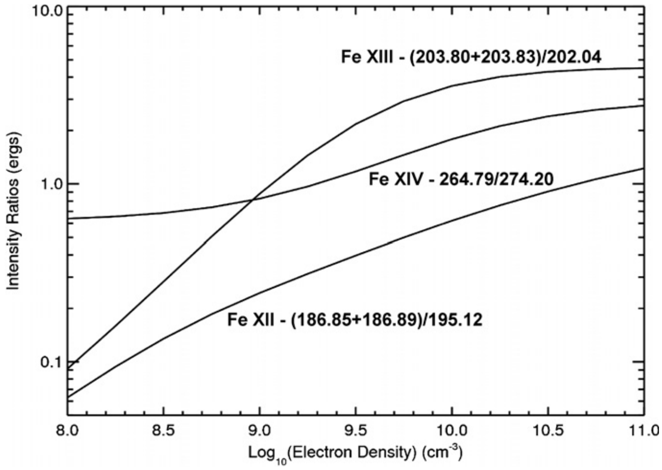

Figure 15. Electron density sensitive line ratios for Fe XII, Fe XIII and Fe XIV coronal ions (from CHIANTI).

point at which all the curves intersect, then this means that a single temperature and emission measure, i.e. an isothermal plasma, can account for all the measured intensities. In practice an isothermal plasma will show intersections over a small area of the plot due to uncertainties in atomic data and/or measurement uncertainties. This technique for investigating emission measure distributions was first developed by Jordan *et al* (1987).

Such a plot for SUMER spectra obtained above the limb is shown in figure 14 (from Warren and Warshall 2002). The different curves are from the spectral lines of Si ions ranging from Si VII to Si XII, so solar abundances are not a factor in the plot. More recent observations with EIS spectra indicate that there may also be a weak higher temperature component in addition to the dominant million degree isothermal component (Warren and Brooks 2009). The data in figure 14 strongly support an isothermal corona.

On the disc coronal loops in active regions fall into two classes: hot loops near 2–3 $\times$ 10^6 K and warm loops with temperatures about 1.4 $\times$ 10^6 K. The warm loops surround a core of hot loops. The hot loops can be explained by loop heating models that provide steady heat input into the loops. The warm loops can only be explained by models that put heat into the loops impulsively. Spectroscopy is the key tool for understanding how the loops are heated. Currently there is much work being done to understand the physics of coronal loops (e.g. Cirtain *et al* 2007, Warren *et al* 2008, Tripathi *et al* 2009, Patsourakos and Klimchuk 2009).

To understand the role of spectroscopy, consider the basics of any loop-heating model. The models consist of plasma confined by a magnetic field into a loop whose cross-sectional area may be tapered towards the footpoints. Heat is put into the plasma according to various assumptions. The heat energy is lost through conduction along field lines into the chromospheric lower boundary of the loop, which is basically a heat sink because the energy input is small compared to the internal chromospheric energy. The heat is also lost via radiation in the corona, which is proportional to the square of the electron density. The heated chromosphere at the base of the loop may evaporate plasma into the loop thus raising its density in the corona. The plasma behaviour after heat injection is governed by the conservation equations of mass, momentum and energy. Since the heating mechanism of a loop is not yet understood, heat may be put into the loop model at any location, or at random locations, and may be either steady in time or in the form of impulses.

To test any given model, it is necessary to be able to measure the temperature distribution in the loop and in particular the electron density since it is the only way to calculate a radiative energy loss rate. Thus loops are observed in spectral lines emitted in both the transition region and corona whenever possible, and line ratios are used to obtain densities whenever possible. The strong coronal emission lines in the 170–300 Å bandpass observed by EIS are adequate for observing well the coronal emission. There are some transition region diagnostics, but they are limited below 300 Å.

Good coronal electron density diagnostics are available in the EIS range from Fe XII, Fe XIII and Fe XIV (see figure 15 for electron densities typically encountered in solar coronal regions). By far the most sensitive ratio is the Fe XIII ratio. The Fe XII and Fe XIII ratios do not yield the same densities for the highest densities observed in active regions and flares, i.e. above about 10^{10} cm^{-3} (e.g. Young *et al* 2009). The Fe XII densities are higher by about a factor of 3. At low densities there is fair agreement between the two diagnostics. The reason for this difficulty is not yet understood but seems due to the atomic data in one way or another. The atomic data for these iron ions are extensive because of the large number of configurations and levels involved in all the calculations. We strongly encourage atomic physicists to revisit the atomic data for Fe VIII–Fe XVI for spectral lines in the EUV above about 170 Å.

Tests of loop-heating models for so-called warm active region loops show that steady heating cannot account for the high electron densities in the loops (e.g. Warren *et al* 2008). On the other hand, impulsive models cannot account for

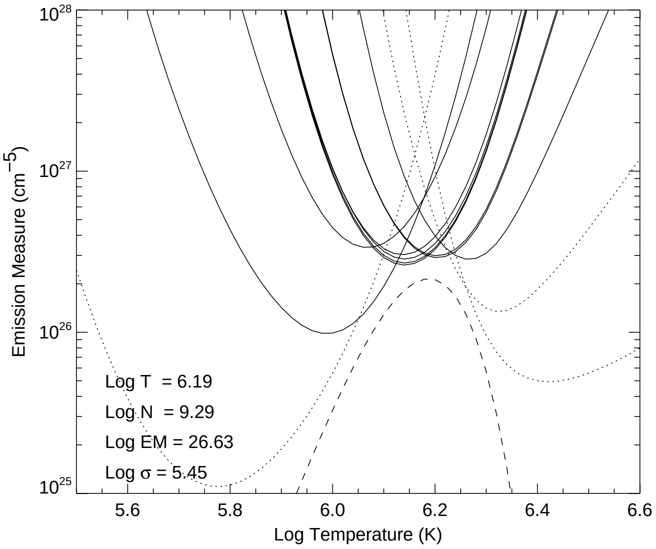

Figure 16. Emission measures as a function of temperature for a set of spectral lines emitted by a small loop segment. The dashed curve is the emission measure distribution that accounts for all the observed intensities (from Warren H P *et al* 2008 *Astrophys. J.* **686** L131).

the observed lifetimes (much longer than radiative lifetimes) unless the overall loop envelope is regarded as composed of unresolved thin magnetic threads, which are heated sequentially. In this scenario the overall loop intensity curves can be reproduced as a function of time and the high densities can be accounted for. Measurements of filling factors, e.g. the fraction of observed path length or volume actually emitting plasma, are around 20% for high-density loops (Warren *et al* 2008), a direct observational confirmation of unresolved structures in the corona.

The evolution of loops, i.e. their heating and cooling, provides another test of loop-heating models. Active regions have two loop populations: a hot loop population in the active region cores (2–3 $\times$ 10^6 K) and a periphery population of so-called warm loops that have temperatures of about 0.4–1.3 $\times$ 10^6 K (e.g. Ugarte-Urra *et al* 2009). On-going studies of the cooling of these loops (above reference) promises to shed much light on loop-heating models.

Another result from testing loop-heating models is that unlike the off-limb coronal results for the warm temperature corona discussed above, the loops observed as they cool on the disc are not isothermal. However, they have an emission measure distribution that has a narrow spread in temperature, i.e. a few hundred thousand degrees (see figure 16 from Warren *et al* (2008)). Thus the unresolved threads must cool together, but not quite at the same temperature. Figure 16 shows a set of spectral line emission measures as a function of temperature for a small active region loop segment at a given instant of time observed by EIS. The curves do not all intersect at a single point and therefore the plasma is not isothermal. However, the curves intersect not too far from each other which implies only a small spread of temperatures for the emitting plasma. The dashed curve is an emission measure distribution, assumed Gaussian, that accounts for all the observed line intensities.

Another interesting recent result from EIS coronal EUV spectroscopy is the observation of outflows over large areas of active regions where the emission is actually faint (e.g. Doschek *et al* 2007, Harra *et al* 2008, Baker *et al* 2009). Similar outflows have been previously reported from SUMER observations (e.g. Marsch *et al* 2004). The situation is illustrated in figure 17. The left image is the intensity of the active region in the spectral line of Fe XII at 195.12 Å. The right panel is an image of the centroid of this spectral line. White indicates no net Doppler speed, blue is the outflow towards the observer and red is the inflow towards the chromosphere. Typical outflow speeds are 15–20 km s^{-1} but sometimes there is an additional component indicating outflow speeds up to 200 km s^{-1} (Bryans *et al* 2010). The outflows are sometimes visible even at high temperatures (e.g. Fe XV) and the spectral lines are wide, indicating either considerable random mass motions or unresolved flows from multiple sources. The flows persist for days.

Previously, very bright coronal rays at distances up to 2.5 solar radii, possibly associated with outflows from active regions, were observed in 2002 with the *CORONAS-F* SPIRIT telescope coronagraph in the EUV 175 Å band (Fe IX-X-XI lines) (Slemzin *et al* 2008). Some of the rays had counterparts in the white-light LASCO-C2 image. SPIRIT was the first telescope to investigate the inner corona in an enhanced coronagraphic mode with the solar disc obscured by an occulter.

The origin of these outflows, and their relevance to coronal physics, is still unclear. The magnetic field configuration below the outflows is mainly monopolar, indicating either open magnetic flux tubes or long loops that connect distant regions on the Sun. If the field lines are open, the outflows might make a considerable contribution to the solar wind. Work is on-going to connect the outflows seen near the Sun with *in situ* solar wind data obtained near the Earth.

Spectroscopy of the inner corona can be used in a limited way to detect the presence of non-thermal particles, i.e. a departure from a Maxwellian velocity distribution. We have already noted some results for the transition region in section 3. Although the excitation rate coefficients C used to calculate the upper level populations of spectral transitions are integrals over the excitation cross section and velocity distribution, i.e.

$$C_{i,j} = \int_{V_T}^{\infty} v\sigma_{i,j}(v) f(v)\,\mathrm{d}v \ (\mathrm{cm}^3\ \mathrm{s}^{-1}), \tag{5}$$

where v is the electron velocity, V_T is the velocity for threshold of excitation between the lower level i and the upper level j and $f(v)$ is the velocity distribution, usually assumed to be Maxwellian, the presence of a high-temperature tail on a Maxwellian is detectable by using lines very sensitive to high-energy excitation. The intensity ratio of a high-energy excitation line to the intensity of a line produced by electrons with energies near the peak of the velocity distribution is temperature sensitive through the function $\exp(-\Delta E/kT_e)$, where ΔE is the energy difference, k is Boltzmann's constant and T_e is the electron temperature. If the emission measure distribution can be found using only lower excitation lines,

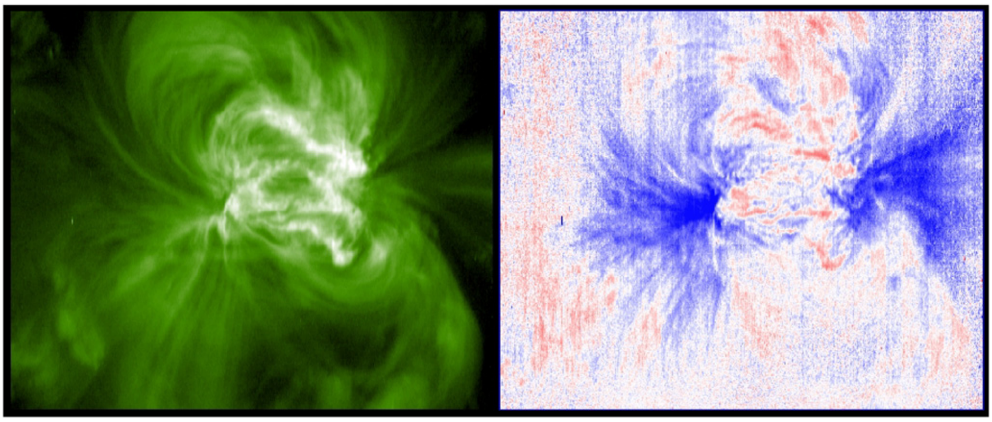

Figure 17. Left panel: EIS raster intensity image of an active region in Fe XII 195 Å. Right panel: the Fe XII centroid image. Blue is Doppler outflow; red is Doppler inflow towards the Sun.

then the emission measure calculated from higher excitation lines gives an indication of the existence of a non-thermal component, i.e. if the high excitation emission measure is much greater than the emission measure computed from the low excitation lines, then a high-energy non-thermal velocity component is indicated.

Unfortunately it is difficult to find many suitable line ratios in the UV and EUV. Although it is easy to find high-energy lines, they usually differ greatly in wavelength from the most desirable comparison lines (e.g. O VI, 150 Å 3p–2s (high energy) and 1032, 1038 Å 2p–2s (low energy) lines). In these cases two different instruments are frequently required to make a measurement. However, there are a few cases where lines can be closer together, within the range of a single instrument. For example, the Na isoelectronic sequence supplies some useful temperature diagnostics for the transition region (Mg, Al, Si). (The Mg lines fall at wavelengths greater than 2000 Å.) The high-excitation line is a 3d–3p transition where the 3d upper level is excited from the ground state 3s level. The 3d–3p line is generally not too far in wavelength from the low energy 3p–3s transition. The He-like ion has a singlet and triplet system. For example, for O VII excitation to the 1s2p ^{3}P levels at wavelengths near 22 Å can result in a 1s2p ^{3}P transition to 1s2s ^{3}S, which produces spectral lines near 1638 Å. These lines can be used to get emission measures for comparison to emission measures obtained from lower energy excited lines. A further example is Fe XVII, which produces excitations equivalent to about 15–17 Å but can result in EUV lines at wavelengths such as 254 Å due to the excitation and decay processes: 2p to 3p to 3s and 2p to 3d to 3p. Several of these lines have been observed by EIS.

So far, the work done in searching for non-thermal coronal particles has lead to contradictory and somewhat ambiguous results. Some current work is Muglach *et al* (2010), Ralchenko *et al* (2007) and Feldman *et al* (2007).

5. Spectroscopy: solar flares

Solar flares produce multi-million degree plasma that can reach thermal temperatures as high as 40×10^6 K. Flares emit x-rays and the solar x-ray spectrum provides excellent diagnostics for measurements of temperature, ion abundances and dynamics.

Below about 10 Å the dominant line emission is due to transitions in He-like and H-like ions and associated collisionally and dielectronically excited satellite transitions (e.g. Doschek 1990, Gabriel 1972). The satellite transitions become stronger for the heavier elements because of a branching factor involving radiative and autoionization rates and they are important as temperature diagnostics when combined with the intensity of a line produced by electron impact collisional excitation. The satellite lines are most important for elements with atomic number greater than about 14. In the solar case, they are most useful for Ca and Fe spectra (see figure 18). In figure 18 the lettering of transitions was introduced by Gabriel (1972) in order to facilitate discussions of the spectra.

As an example, consider the excitation of the resonance line of a He-like ion, called line w (see figure 18), due to electron impact excitation, i.e.

$$X(1s^2\,{}^1S_0) + e_0 \rightarrow X(1s2p\,{}^1P_1) + e_1, \tag{6}$$

$$X(1s2p\,{}^1P_1) \rightarrow X(1s^2\,{}^1S_0) + (h\nu)_w, \tag{7}$$

where e_0 and e_1 represent the electron at different energies before and after the collision, respectively. A useful dielectronic line, called line j, is formed as follows:

$$X(1s^2\,{}^1S_0) + e \rightleftharpoons X(1s2p^2\,{}^2D_{5/2}), \tag{8}$$

$$X(1s2p^2\,{}^2D_{5/2}) \rightarrow X(1s^2 2p\,{}^2P_{3/2}) + (h\nu)_j. \tag{9}$$

In equation (8), the left–right arrows indicate that the doubly excited Li-like ion 1s2p^2 ^{2}D$_{5/2}$ state could autoionize as well as radiatively stabilize. The point is that the formation of both lines w and j begins with the same state of the He-like ion, and therefore the intensity ratio does not depend on any ion abundance. The intensity ratio I_j/I_w is temperature sensitive with the dependence

$$I_j/I_w = A\exp(-(E_s - E_0)/kT_e)/T_e, \tag{10}$$

where E_s is the energy difference between the ground state He-like ion and the doubly excited state, E_0 is the resonance

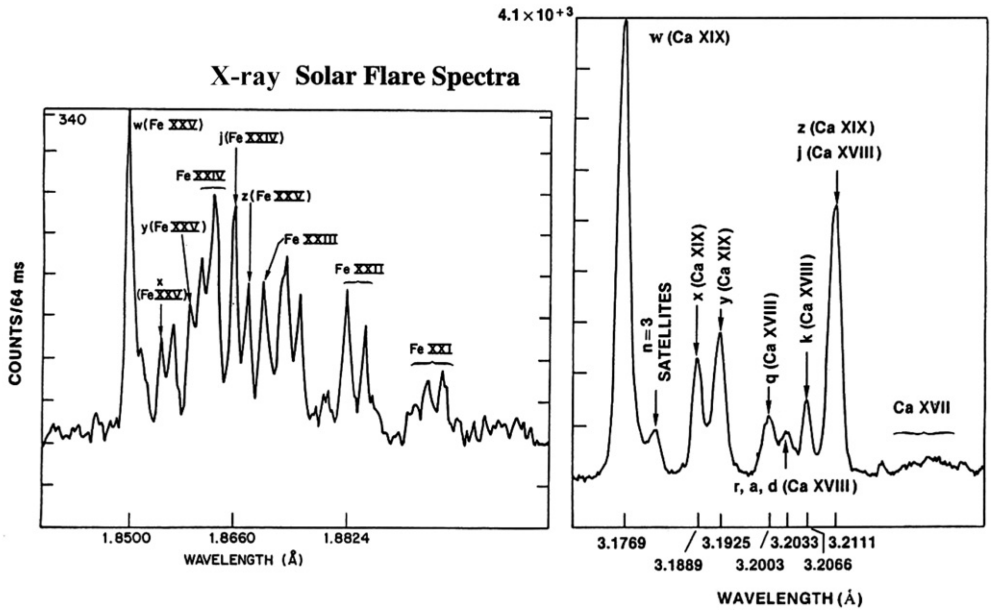

Figure 18. Left panel: Fe solar flare spectrum from the NRL BCS on the US Department of Defense P78-1 spacecraft (e.g. Doschek 1983). Lines w, x, y and z belong to the singlet and triplet systems of the He-like ion. Line q is an inner-shell electron impact excited satellite line; most of the others are produced by dielectronic capture followed by radiative stabilization. Right panel: the same for a Ca flare spectrum.

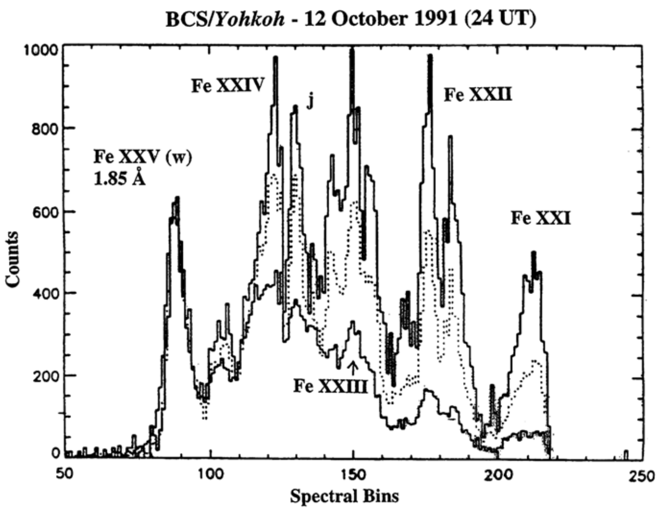

Figure 19. Fe spectra from the BCS spectrometer package on *Yohkoh*. The three spectra have been normalized to the intensity of the Fe XXV resonance line called line w.

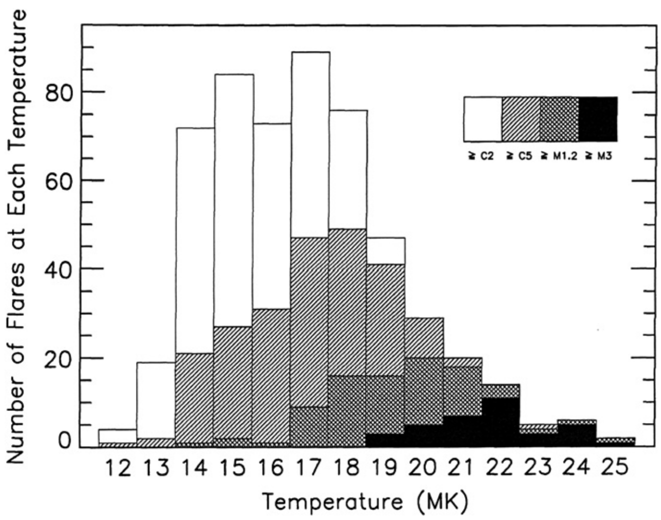

Figure 20. Histogram of flare temperature distributions for flares of different classifications. X-flares are the most intense, followed by M-flares, C-flares, B-flares and then A-flares. Each class is separated from adjacent classes by one order of magnitude of intensity in the *GOES* environmental broadband x-ray detectors that operate at wavelengths less than about 4 Å (from Feldman *et al* 1995).

line excitation energy and A is a proportionality constant. The above function is quite sensitive to temperature for Fe and Ca spectra, allowing us to estimate flare temperatures (e.g. Feldman *et al* 1995).

As a flare evolves, the x-ray spectra change dramatically in response to temperature. Figure 19 shows spectra from a cooling flare plasma recorded by the BCS package on the *Yohkoh* spacecraft. The spectra are normalized to the resonance line w of Fe XXV. The hottest spectrum is the one with the weakest emission from ions such as Fe XXI. A summary of flare temperatures as a function of flare classification derived from BCS observations from *Yohkoh* by Feldman *et al* (1995) is shown in figure 20. Normally flare temperatures do not exceed around 23×10^6 K for the bulk of the thermal flare plasma. However, Fe XXVI observations reveal a superhot component near 40×10^6 K (e.g. Tanaka 1986). There is no explanation for the limiting temperature of the soft x-ray emitting flare. Flares on other stars can be much hotter.

In addition to temperature information, Bragg crystal x-ray spectra have revealed much about chromospheric evaporation in flare loops and random non-thermal mass motions (e.g. Doschek 1990, Harra *et al* 2001, Warren and

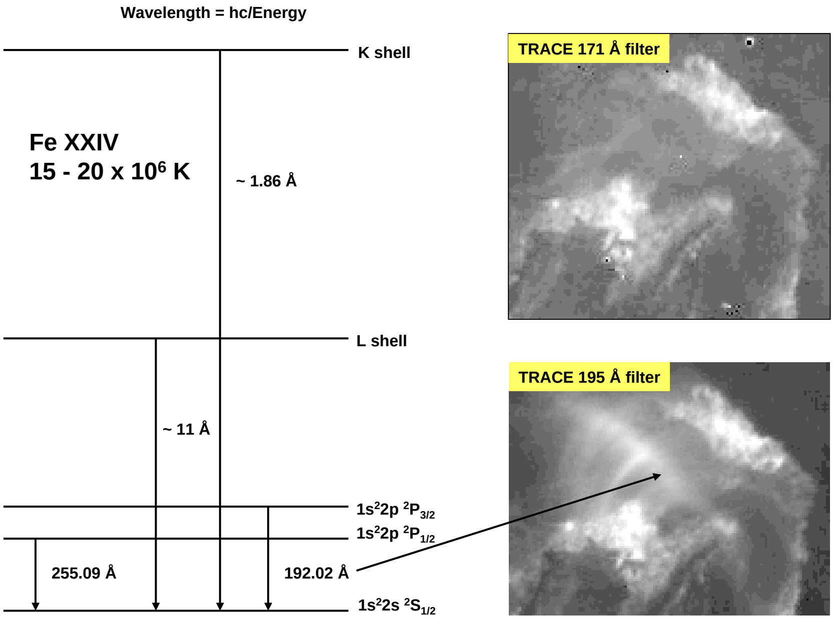

Figure 21. Energy level diagram for Fe XXIV and two flare images from TRACE. There are many K shell and L shell transitions from different levels. The K shell transitions are mainly dielectronic lines, but there are also some inner-shell lines.

Doschek 2005). At the onset of flares spectral lines are quite wide, indicating turbulent speeds of about 150 km s^{-1} that decrease monotonically as the flare brightens in soft x-rays. Also, there is frequently a blueshifted component in the profiles of the x-ray lines during the rise phase of flares that is a signature of chromospheric evaporation. This component also decreases as the flare brightens. Upflow speeds can be quite high, ranging from a few kilometers per second to speeds on the order of 900 km s^{-1}. The plasma moving at speeds greater than about 300 km s^{-1} is closely correlated with the onset of hard x-ray bursts due to thick target bremsstrahlung produced by non-thermal particles produced in the corona impinging on the chromosphere (e.g. Bentley *et al* 1994).

Because the x-ray spectra have no spatial resolution, the sources of evaporation cannot be related to images of flaring loops. However, Czaykowska *et al* (1999) related blueshifts in CDS spectra with both upflows and downflows in loops in both transition region and coronal lines that occurred during the late gradual phase of a flare.

Finally, it must be mentioned that spectral lines from highly ionized elements occur throughout the UV and EUV spectra. The long wavelength transitions are a combination of allowed, forbidden and intersystem lines. Figure 21 illustrates the case for Fe XXIV. The Fe XXIV lines have been useful even in broadband data from spacecraft such as TRACE, and are now being used to analyse EIS flare spectra. Note that significant bright areas of emission in the 195 Å filter image are missing from the 171 Å filter image. This is due to the presence of the 192 Å Fe XXIV line in the 195 Å filter bandpass. There is no equivalent hot line in the 171 Å bandpass. The longest wavelength lines arise from forbidden transitions. A list of some prominent forbidden lines from high iron ionization stages is given in table 4.

Table 4. Some EUV flare forbidden lines.

Ion	Wavelength (Å)	Transition
Fe XVII	1153.20	$2p^5 3s\, ^3P_1$–$2p^5 3s\, ^3P_0$
Fe XVIII	974.86	$2s^2 2p^5\, ^2P_{3/2}$–$2s^2 2p^5\, ^2P_{1/2}$
Fe XIX	1118.06	$2s^2 2p^4\, ^3P_2$–$2s^2 2p^4\, ^3P_1$
Fe XXI	1354.08	$2s^2 2p^2\, ^3P_0$–$2s^2 2p^2\, ^3P_1$
Fe XXII	845.55	$2s^2 2p\, ^2P_{1/2}$–$2s^2 2p\, ^2P_{3/2}$
Fe XXIII	1079.3	$2s2p\, ^3P_1$–$2s2p\, ^3P_2$

6. The first ionization effect

We conclude the spectroscopy discussion by discussing a subject that involves all regions of the solar upper atmosphere. Table 1 reveals that photospheric and coronal abundances are different for certain elements. The elements that have first ionization potentials below about 10 eV, such as Mg, Si and Fe, are more abundant in the quiet corona by about a factor of 4 than elements with relatively high first ionization potentials such as Ar and Ne. This seems quite strange because the corona is hot and all elements are ionized. Thus it is clear that the coronal composition is somehow governed by physical effects that occur low in the atmosphere, perhaps in the chromosphere, where the atmosphere is still relatively cool and neutral elements can still exist. The seminal papers by Meyer (1985a, 1985b) did much to bring this effect to the attention of solar spectroscopists.

Subsequently the FIP effect has been used to investigate all regions of the atmosphere. For example, it has been found that in open flux regions, such as coronal holes that produce the fast solar wind, the coronal abundances are near-photospheric, but in closed magnetic regions, such as coronal loops, the coronal abundances are enhanced in low FIP elements. Even more interestingly, emerging magnetic flux in the photosphere,

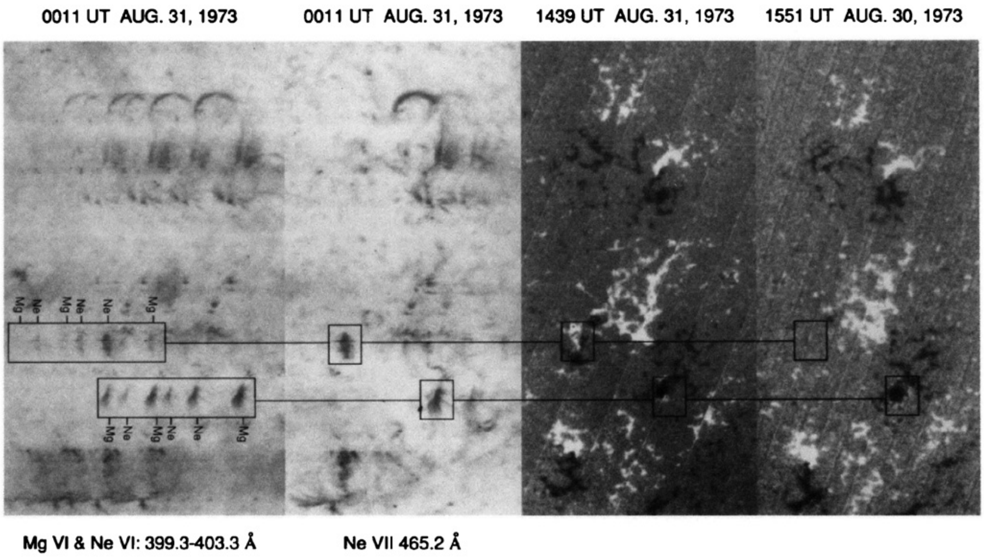

Figure 22. Spectral images showing coronal structures in multiplets of Ne VI and Mg VI from the slitless spectrograph on the *Skylab* manned space station. The spectra are related to ground-based magnetograms (right) which show the magnetic field where black and white differentiate different line-of-sight polarities (from Sheeley 1995).

which produces coronal loops, shows a temporal FIP effect depending on how old the emerging regions are (e.g. Sheeley 1995). Initially, young coronal loops show photospheric abundances, which gradually evolve towards coronal low FIP enhanced abundances.

The temporal FIP effect is illustrated dramatically in figure 22, which shows spectral images of multiplets of Ne VI (high FIP) and Mg VI (low FIP) and their relationship to magnetic flux regions on two successive days. The bottom-most boxed multiplet shows that the Mg VI lines are stronger than the Ne VI lines. The magnetograms in the right-hand part of the image show that this region is relatively old because the magnetic region looks almost the same on both days. However, the top-most boxed multiplet shows that the Ne VI lines are much stronger than the Mg VI lines, and the magnetic region that is obvious on 31 August is barely visible on 30 August. This upper region is a newly emerging region. The differences in intensities between the two regions are most likely due to abundance changes, because the contribution functions of Mg VI and Ne VI are quite similar, i.e. a change in the temperature distribution will have only a small effect on the intensity ratios of the Ne and Mg lines, for emission measure distributions that are typical of quiet Sun features on the solar disc. The FIP effect is a valuable tool for investigating different types of coronal structures, even without understanding the physics behind its origin.

The FIP effect in flares has given contradictory results (e.g. compare Feldman and Widing 1990, Schmelz 1993, Fludra and Schmelz 1995). Currently, perhaps a good summary is to say that the FIP effect appears to give abundances somewhere between photospheric and coronal but possibly variable (e.g. Sterling *et al* 1993). Measurements of the Ar/Ca abundance always give values smaller (e.g. Doschek *et al* 1985, Antonucci *et al* 1987) than in the photosphere (1.15, Asplund *et al* 2009). This supports at least a partial coronal abundance interpretation.

The reason for the FIP effect is under continual investigation. The theory by Laming (2004) explains not only solar FIP phenomena, but also stellar FIP phenomena where an inverse FIP effect is sometimes observed (e.g. Brinkman *et al* 2001, Laming and Hwang 2009). The Laming (2004) model explains the FIP effect as the result of a pondermotive force due to Alfven waves in the chromosphere. The Laming model as well as other models is still currently being tested. If the Laming (2004) theory is correct, then the FIP effect can be used to investigate wave phenomena in the atmosphere, another potentially very useful application of the effect. Recently, Wood and Linsky (2010) have found a correlation between the FIP effect and spectral type in stellar spectra from the *CHANDRA* x-ray astronomy spacecraft. Perhaps the stellar spectra will be key in reaching a final understanding of the FIP effect.

7. The future of solar x-ray–EUV spectroscopy

Solar x-ray–EUV spectroscopy is just beginning to fulfil its high potential for understanding the solar atmosphere. It is only recently that spectra can be obtained with both high spatial and spectral resolution from which images can be constructed in a reasonably short-time period. However, the time resolution of spectral imaging still needs to be improved. And in spite of the current high spatial resolution obtained by, for example, EIS (2″), the chromosphere and transition region still remain unresolved. Although EVE will address some of the time resolution issues and provide new flare diagnostics, spatial resolution of the order of 0.2″ is needed to track energetic phenomena from the photosphere into the corona and out into the heliosphere. As mentioned in section 2, the upcoming NASA Small Explorer Mission called IRIS will do much to address the poor resolution in the chromosphere and lower transition region, but will still not provide this resolution for the upper transition region and corona. It is now believed by many that the corona is still spatially unresolved at 1.0″ (TRACE) due to unresolved threads in loops, and therefore it is highly desirable to have 0.2″ resolution all the way from the photosphere into the corona. None of the instruments listed in table 2 have the spatial resolution that appears necessary to resolve adequately the structures in the solar transition region and corona. The best available spatial resolution for the instruments in table 2 is about 1400 km, or 2″.

There are a number of spectroscopic issues that need to be resolved in order to understand the much higher quality and quantity of data now being obtained from solar space spectroscopic instrumentation. Below we highlight a few of them.

(1) The spectra of the solar atmosphere obtained in two limited EUV wavelength bands from EIS reveal that about half of the lines seen are not yet identified (Brown *et al* 2008). So a new surge in pure laboratory atomic spectroscopy is needed in order to fully identify the spectra. Also, comparisons of plasma diagnostic calculations involving some prominent solar lines of Fe have revealed apparent inconsistencies in atomic data. Iron ions such as Fe XII are difficult theoretical subjects because of the myriad levels and configuration interactions involved and therefore we need highly detailed atomic models to make accurate intensity predictions. Thus, concurrent with the pure spectroscopy, deeper investigations of the atomic physics of the ions useful for solar density diagnostics are needed.

However, no matter how detailed the atomic models become, it is highly desirable to obtain experimental laboratory verification of ionization balance calculations and atomic parameters such as rate coefficients and spontaneous decay rates. The measurements are often difficult and time consuming, but experimental verification is the only way to be sure of the atomic physics. So far, works with devices such as the electron beam ion trap (EBIT) have made enormous contributions to the atomic physics for different ions and elements (e.g. Beiersdorfer 2009), and works on dielectronic recombination rates, the most uncertain quantity in the ionization balance calculations, have provided key guidance in helping to interpret the solar atomic data (e.g. Savin and Laming 2002, Savin *et al* 2006). Work on improving the ionization balance calculations is a continuing effort.

(2) From observations it is known that the temperature from the base of the upper transition region to the top of the non-flaring corona spans the 2×10^5–3×10^6 K domain. Typical depictions in the literature of the emission measure distributions in that region indicate that the emission measure varies slowly with temperature. But recent studies of the emission measure distribution from line intensities acquired by well-calibrated spectrometers show four peaks that appear as if they are the result of nearly isothermal plasmas with temperatures of about 4×10^5, 8×10^5, 1.2×10^6 and 3×10^6 K (Feldman and Landi 2008). It is not easy to understand this unique emission measure distribution solely from the nature of the energy deposition. Perhaps the behaviour is connected with the radiative loss properties of the plasma which are a direct result of the atomic physics properties of the coronal abundant elements.

(3) As discussed in section 4, the intensity ratio of a line originating from a high excitation level (E_h) to a line originating in a low excitation level (E_l) within the same ion is proportional to

$$R \sim T_e^{-1/2} \exp(-(E_h - E_l)/kT_e), \qquad (11)$$

where k is the Boltzmann constant, and T_e is the electron temperature. For the system to be useful as a diagnostic tool it is best that the term within the exponential be $\geqslant 1$ and that the two lines appear in close wavelength proximity. The Na-like lines mentioned in section 4 are a good example. For solar diagnostics the relevant transitions in Mg II and Si IV are useful. However, at the higher ionization stages the value of $(E_h - E_l)$ becomes smaller than kT_e, and the diagnostic becomes insensitive. For example, for Ar VIII $(E_h - E_l)/kT_e \sim 0.7$ and in Fe XVI it is reduced to ~0.2.

There are also other line ratios that can be used for determining the temperature of solar plasmas where the lines are relatively close in wavelength. These lines are produced by forbidden transitions in the ground configuration of Li-like to F-like ions (i.e. $2s^22p^kU$–$2s^22p^kL$) and the excited transition of the type ($2s^22p^{k-1}3p$–$2s^22p^{k-1}3s$) or ($2s^22p^{k-1}3d$–$2s^22p^{k-1}3p$). For ions that are 6 to 10 times ionized the two sets of transitions provide diagnostic lines in the 1000 Å range that are observed by SUMER. For some of these ions, the exponential factor is $\geqslant 1$, rendering these lines a potential diagnostic system. However, unfortunately the atomic calculations for these systems are not satisfactory. Improvement here is highly desirable.

(4) Long ago it was recognized that the intensities of the He II lines are much enhanced relative to their expected intensities when plasma in a steady state and a Maxwellian electron distribution are assumed. Over the years many attempts were made to understand the enhancements, with varying degree of success (e.g. Jordan 1975, 1980, Macpherson and Jordan 1999, Pietarila and Judge 2004). A recent attempt (Feldman *et al* 2010), which assumes an electron distribution consisting of two Maxwellian distributions, one at the temperature of maximum He^+ population and a second with a minute ($\sim 10^{-4}$) fraction at a temperature of $kT_e \pm 100$ eV, produced interesting results. Clearly much more work needs to be put into investigating cases involving intensities of lines originating in very high energy levels.

(5) A comparison between the appearances of structures in the Fe VII, Fe VIII and possibly Fe IX lines and those from lighter elements indicates that the temperatures of maximum ion fractions in these ions are lower than predicted assuming ionization equilibrium. More work needs to be done on the ionization equilibrium calculations for these Fe ions. For some of the ions where a significant fraction of the ion population is in excited

levels, the electron density is an important factor in the equilibrium calculations.

(6) Using line intensities recorded by SUMER, the temperature of quiet coronal structures as seen above the limb during solar minimum periods was found to be 1.3–1.4 $\times$ 10^6 K. However, temperatures of similar regions derived using the CDS on *SOHO* and EIS are about 10–15% lower. The reason for this discrepancy is as yet unclear but again implicates the atomic physics. For example, SUMER operates in a relatively long wavelength range where many of the lines used in the analysis originate within the ground configuration and from spin forbidden transitions between the first excited configuration and the ground configuration. The elements contributing to the lines used in the analysis belong mostly to the third row of the periodic table, i.e. Na to Ar. CDS and EIS operate at significantly lower wavelengths where nearly all the lines result from allowed transitions. Moreover, while the lines in the SUMER spectra originate in the relative low Z elements the lines in CDS and EIS are emitted by Fe ions.

(7) Emission measures derived from lines emitted by Li-like ions result in values that are about one-half of the values that are derived from lines emitted by other ions. The reason for this discrepancy, known for about 40 years, is still unclear.

(8) As mentioned, it is highly desirable to experimentally check in the laboratory theoretical atomic calculations. EBITs and tokamaks could be used to test some of the calculations. Any laboratory device that generates plasmas at approximate solar temperatures and densities might be useful for this purpose if the physical layout allows a high resolution spectrometer to observe the plasma. There is currently much interest in the synergies provided by laboratory plasmas and solar plasmas involving a wide range of plasma physics and observational diagnostics (e.g. Dahlburg *et al* 2010).

In summary, the recent solar spectral observations at x-ray and EUV wavelengths are providing new impetus to revitalize laboratory and theoretical atomic spectroscopy as well as attempts to check theoretical calculations using laboratory plasma devices.

Finally, readers are directed to more detailed works on solar physics and solar spectroscopy if they desire to delve into the subject more thoroughly. As examples of sources, we recommend Phillips *et al* (2008), Aschwanden (2005) and Mariska (1992).

Acknowledgments

The authors acknowledge support from the NASA *Hinode* program and from ONR/NRL 6.1 basic research funds. *Hinode* is a Japanese mission developed and launched by ISAS/JAXA, collaborating with NAOJ as domestic partner, and NASA (USA) and STFC (UK) as international partners. Scientific operation of the *Hinode* mission is conducted by the *Hinode* science team organized at ISAS/JAXA. This team mainly consists of scientists from institutes in the partner countries. Support for the post-launch operation is provided by JAXA and NAOJ, STFC, NASA, ESA (European Space Agency) and NSC (Norway). We are grateful to the *Hinode* team for all their efforts in the design, build and operation of the mission.

References

Acton L W *et al* 1980 *Sol. Phys.* **65** 53
Antonucci E, Marocchi D, Gabriel A H and Doschek G A 1987 *Astron. Astrophys.* **188** 159
Aschwanden M 2005 *Physics of the Solar Corona* (Berlin: Springer)
Asplund M, Grevesse N, Jacques Sauval A and Scott P 2009 *Ann. Rev. Astron. Astrophys.* **47** 481
Baker D, van Driel-Gesztelyi L, Mandrini C H, Demoulin P and Murray M J 2009 *Astrophys. J.* **705** 926
Bartoe J-D F, Brueckner G E, Purcell J D and Tousey R 1977 *Appl. Opt.* **16** 879
Beiersdorfer P 2009 *Phys. Scr.* T **134** 1
Bentley R D *et al* 1994 *Astrophys. J.* **421** L55
Berger T E, De Pontieu B, Schrijver C J and Title A M 1999 *Astrophys. J.* **519** L97
Bonnet R M *et al* 1978 *Astrophys. J.* **221** 1032
Brekke P, Hassler D M and Wilhelm K 1997 *Astrophys. J.* **175** 349
Brinkman A C *et al* 2001 *Astron. Astrophys.* **365** 324
Brown C M, Feldman U, Seely J F, Korendyke C M and Hara H 2008 *Astrophys. J. Suppl. Ser.* **176** 511
Brueckner G E and Bartoe J-D F 1983 *Astrophys. J.* **272** 329
Bruner E C Jr 1977 *Space Sci. Instrum.* **3** 369
Bruner E C Jr and McWhirter R W P 1979 *Astrophys. J.* **231** 557
Bryans P, Landi E and Savin D W 2009 *Astrophys. J.* **691** 1540
Bryans P, Young P R and Doschek G A 2010 *Astrophys. J.* **715** 1012
Chae J, Schuhle U and Lemaire P 1998b *Astrophys. J.* **505** 957
Chae J, Yun H S and Poland A I 1998a *Astrophys. J. Suppl.* **114** 151
Cirtain J W, Del Zanna G, DeLuca E E, Mason H E, Martens P C H and Schmelz J T 2007 *Astrophys. J.* **655** 598
Culhane J L *et al* 1991 *Sol. Phys.* **136** 89
Culhane J L *et al* 2007 *Sol. Phys.* **243** 19
Czaykowska A, De Pontieu B, Alexander D and Rank G 1999 *Astrophys. J.* **521** L75
Dahlburg J *et al* 2010 *Energies* **3** 1014
Dahlburg R B, Liu J-H, Klimchuk J A and Nigro G 2009 *Astrophys. J.* **704** 1059
De Pontieu B, McIntosh S W, Hansteen V H and Schrijver C J 2009 *Astrophys. J.* **701** L1
Dere K P, Landi E, Young P R, Del Zanna G, Landini M and Mason H E 2009 *Astron. Astrophys.* **498** 915
Doschek G A 1983 *Sol. Phys.* **86** 9
Doschek G A 1984 *Astrophys. J.* **279** 446
Doschek G A 1990 *Astrophys. J. Suppl.* **73** 117
Doschek G A 2006 *Astrophys. J.* **649** 515
Doschek G A, Feldman U and Bohlin J D 1976 *Astrophys. J.* **205** L177
Doschek G A, Feldman U and Seely J F 1985 *Mon. Not. R. Astron. Soc.* **217** 317
Doschek G A, Mariska J T, Warren H P, Brown C M, Culhane J L, Hara H, Watanabe T, Young P R and Mason H E 2007 *Astrophys. J.* **667** L109
Dowdy J F Jr, Rabin D and Moore R L 1986 *Sol. Phys.* **105** 35
Feldman U 1983 *Astrophys. J.* **275** 367
Feldman U and Doschek G A 1977 *Astrophys. J.* **216** L119
Feldman U and Doschek G A 2007 *At. Data Nucl. Data Tables* **93** 779
Feldman U, Doschek G A, Mariska J T and Brown C M 1995 *Astrophys. J.* **450** 441
Feldman U, Doschek G A and Seely J F 1988 *J. Opt. Soc. Am.* B **5** 2237

Feldman U, Doschek G A, Schuhle U and Wilhelm K 1999 *Astrophys. J.* **518** 500
Feldman U, Landi E and Doschek G A 2007 *Astrophys. J.* **660** 1674
Feldman U and Landi E 2008 *Phys. Plasmas* **15** 056051
Feldman U, Ralchenko Yu and Doschek G A 2010 *Astrophys. J.* **708** 244
Feldman U and Widing K G 1990 *Astrophys. J.* **363** 292
Fletcher L and De Pontieu B 1999 *Astrophys. J.* **520** L135
Fludra A and Schmelz J T 1995 *Astrophys. J.* **447** 936
Gabriel A H 1972 *Mon. Not. R. Astron. Soc.* **160** 99
Gabriel A H 1976 *Phil. Trans.* A **281** 339
Hansteen V H, De Pontieu B, Rouppe van der Voort L, van Noort M and Carlsson M 2006 *Astrophys. J.* **647** L73
Hansteen V private communication
Harra L K, Matthews S A and Culhane J L 2001 *Astrophys. J.* **549** 245
Harra L K, Sakao T, Mandrini C H, Hara H, Imada S, Young P R, van Driel-Gesztelyi L and Baker D 2008 *Astrophys. J.* **676** L147
Harrison R A 1997 *Sol. Phys.* **175** 467
Harrison R A *et al* 1995 *Sol. Phys.* **162** 233
Harrison R A, Harra L K, Brkovic A and Parnell C E 2003 *Astron. Astrophys.* **409** 755
Innes D E, Inhester B, Axford W I and Wilhelm K 1997 *Nature* **386** 811
Jordan C 1975 *Mon. Not. R. Astron. Soc.* **170** 429
Jordan C 1980 *Phil. Trans. R. Soc.* A **297** 541
Jordan C, Ayres T R, Brown A, Linsky J L and Simon T 1987 *Mon. Not. R. Astron. Soc.* **225** 903
Judge P G and Centeno R 2008 *Astrophys. J.* **687** 1388
Judge P G 2008 *Astrophys. J.* **683** L87
Ko Y-K, Doschek G A, Warren H P and Young P R 2009 *Astrophys. J.* **697** 1956
Kohl J L *et al* 1995 *Sol. Phys.* **162** 313
Laming J M 2004 *Astrophys. J.* **614** 1063
Laming J M and Feldman U 2000 *Phys. Scr.* **61** 222
Laming J M and Hwang U 2009 *Astrophys. J.* **707** L60
Macpherson K P and Jordan C 1999 *Mon. Not. R. Astron. Soc.* **308** 510
Mariska J T 1992 *The Solar Transition Region* (Cambridge: Cambridge University Press)
Marsch E, Wiegelmann T and Xia L D 2004 *Astron. Astrophys.* **428** 629
Mazzotta P, Mazzitelli G, Colafrancesco S and Vittorio N 1998 *Astron. Astrophys. Suppl.* **133** 403
McKenzie D L *et al* 1980 *Astrophys. J.* **241** 409
Meyer J-P 1985a *Astrophys. J. Suppl. Ser.* **57** 151
Meyer J-P 1985b *Astrophys. J. Suppl. Ser.* **57** 173
Muglach K, Landi E and Doschek G A 2010 *Astrophys. J.* **708** 550
Parker E N 1988 *Astrophys. J.* **330** 474
Patsourakos S and Klimchuk J A 2006 *Astrophys. J.* **647** 1452
Patsourakos S and Klimchuk J A 2009 *Astrophys. J.* **696** 760
Peter H 2001a *Astron. Astrophys.* **374** 1108
Peter H 2001b *Space Sci. Rev.* **95** 107
Peter H, Gudiksen B V and Nordlund A 2006 *Astrophys. J.* **638** 1086
Peter H and Judge P G 1999 *Astrophys. J.* **522** 1148
Phillips K J H, Feldman U and Landi E 2008 *Ultraviolet and X-ray Spectroscopy of the Solar Atmosphere* (Cambridge: Cambridge University Press)
Pietarila A and Judge P G 2004 *Astrophys. J.* **606** 1239
Ralchenko Yu, Feldman U and Doschek G A 2007 *Astrophys. J.* **659** 1682
Reeves E M, Huber M C E and Timothy J G 1977 *Appl. Opt.* **16** 837
Reeves K K, Warren H P and Forbes T G 2007 *Astrophys. J.* **668** 1210
Robbrecht E, Patsourakos S and Vourlidas A 2009 *Astrophys. J.* **701** 283
Sandlin G, Brueckner G E and Tousey R 1977 *Astrophys. J.* **214** 898
Savin D W *et al* 2006 *Astrophys. J.* **642** 1275
Savin D W and Laming J M 2002 *Astrophys. J.* **566** 1166
Schmelz J T 1993 *Astrophys. J.* **408** 373
Sheeley N R Jr 1995 *Astrophys. J.* **440** 884
Shestov S V, Kuzin S V, Urnov A M, Ul'yanov A S and Bogachev S A 2010 *Astron. Lett.* **36** 44
Slemzin V, Bougaenko O, Ignatiev A, Kuzin S, Mitrofanov A, Pertsov A and Zhitnik I 2008 *Ann. Geophys.* **26** 3007
Sterling A C, Doschek G A and Feldman U 1993 *Astrophys. J.* **404** 394
Tanaka K 1982 *Astrophys. J.* **254** L59
Tanaka K 1986 *Publ. Astron. Soc. Japan* **38** 225
Tousey R, Bartoe J-D F, Brueckner G E and Purcell J D 1977 *Appl. Opt.* **16** 870
Tripathi D, Mason H E, Dwivedi B N, Del Zanna G and Young P R 2009 *Astrophys. J.* **694** 1256
Ugarte-Urra I, Warren H P and Brooks D H 2009 *Astrophys. J.* **695** 642
Urnov A M, Shestov S V, Bogachev S A, Goryaev F F, Zhitnik I A and Kuzin S V 2007 *Astron. Lett.* **33** 396
Vourlidas A *et al* 2010 *Sol. Phys.* **261** 53
Warren H P, Urra-Ugarte I, Doschek G A, Brooks D H and Williams D R 2008 *Astrophys. J.* **686** L131
Warren H P and Brooks D H 2009 *Astrophys. J.* **700** 762
Warren H P and Doschek G A 2005 *Astrophys. J.* **618** L157
Warren H P and Warshall A D 2002 *Astrophys. J.* **571** 999
Wilhelm K *et al* 1995 *Sol. Phys.* **162** 189
Winebarger A R, Warren H P, van Ballegooijen A, DeLuca E E and Golub L 2002 *Astrophys. J.* **567** L89
Wood B E and Linsky J L 2010 *Astrophys. J.* **717** 1279
Woods T N *et al* 2010 *Sol. Phys.* DOI 10.1007/s1 1207-009-9487-6
Young P R, Watanabe T, Hara H and Mariska J T 2009 *Astron. Astrophys.* **495** 587
Zhitnik I A, Kuzin S V, Oraevskii V N, Pertsov A A, Sobel'man I I and Urnov A M 1998 *Astron. Lett.* **24** 819
Zhitnik I A, Kuzin S V, Urnov A M, Beigman I L, Bozhenkov S A and Tolstikhina I Yu 2005 *Astron. Lett.* **31** 37